OPEN ACCESS
IOP Publishing
Superconductor Science and Technology
Supercond. Sci. Technol. **38** (2025) 125004 (19pp)
https://doi.org/10.1088/1361-6668/ae2362

Robotic winding of non-planar high-temperature superconducting coils

Magnus Dam* and **Tabea Arndt**

Institute for Technical Physics, Karlsruhe Institute of Technology, DE-76344 Eggenstein-Leopoldshafen, Germany

E-mail: magnus.dam@kit.edu

Received 1 August 2025, revised 29 October 2025
Accepted for publication 24 November 2025
Published 4 December 2025

Abstract

The development of non-planar high-temperature superconducting (HTS) coils enables magnet designs that make more efficient use of superconducting material, benefiting applications such as rotating machines, particle accelerators, energy storage systems, and fusion devices. Robotic winding enables consistent, safe, and adaptable construction of such non-planar coil geometries. We present our robotic winding setup consisting of an articulated robot equipped with a specialized winding tool and a synchronized workpiece positioner. We employ a differential geometry approach to design non-planar HTS coil shapes with hard-way bending, in which the mechanical strain remains within material limits. Based on the coil shape, we derive winding tool trajectory and rotations required for robotic execution. We validate our approach by winding a non-planar superellipse-shaped HTS coil and experimentally characterizing its electromagnetic performance.

Keywords: robotic winding, coil shape design, HTS coil, non-planar coil, strain analysis, no-insulation coil, superellipse-shaped coil

1. Introduction

Non-planar coils wound with high-temperature superconducting (HTS) coated conductors are being explored for a variety of magnet configurations. Dipole-type magnets employing non-planar HTS coils include flared-end coils [1], saddle-shaped coils [2, 3], cloverleaf coils [4], and canted cosine theta (CCT) magnets [5, 6]. Force-balanced toroidal coils are being considered for tokamaks [7] and superconducting magnetic energy storage [8], and helical windings are being evaluated for undulators [9]. Most prominently, non-planar HTS coils are being developed for stellarators [10, 11], and rotating machines [12]. The development of non-planar HTS coils expands the integration of HTS technology into applications traditionally dominated by low-temperature superconducting magnets. This advancement enables operation at higher temperatures or generation of stronger magnetic fields, which can enhance performance and efficiency of superconducting systems.

Constructing non-planar coils with HTS tapes poses significant challenges due to the HTS layer's sensitivity to mechanical strain. Winding complex coil shapes without damaging the HTS tape requires guided placement of the HTS tape onto the coil former [13]. To meet this requirement, robotic winding is emerging as a promising solution. Robotic systems offer high-precision control over the winding tool trajectory, ensuring accurate HTS tape placement with minimal handling-induced strain.

Shaping an HTS tape into a non-planar winding induces strain within the tape. A tape can be deformed by three distinct mechanisms, shown in figure 1: (a) easy-way bending,

* Author to whom any correspondence should be addressed.

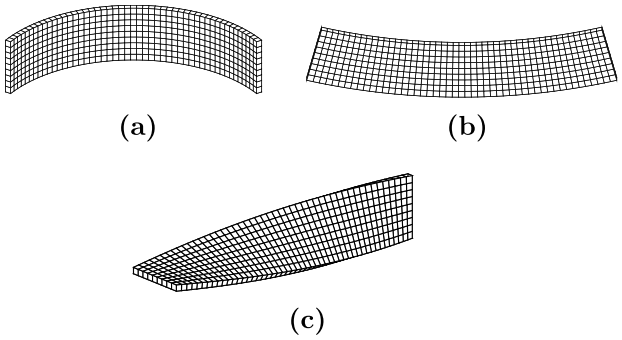

Figure 1. The three deformation mechanisms of HTS tape: (a) easy-way bending, (b) hard-way bending, and (c) twisting.

(b) hard-way bending, and (c) twisting. Easy-way bending is mainly characterized by the normal curvature of the tape's mid-surface and occurs in the direction parallel to the tape's thickness, causing either compression or tension of the HTS layer depending on the bending direction. Hard-way bending is characterized by the geodesic curvature of the tape's mid-surface and it introduces compressive and tensile strain in opposite regions of the HTS layer by bending the tape in the direction parallel to its width [14]. Twisting is characterized by the twist rate of the tape's mid-surface and it rotates the mid-surface around its neutral axis, inducing a shear strain within the tape, where the regions farthest from the rotation axis undergo the greatest strain [15].

The differential geometry approach to coil shape design [16] is a powerful method to control the different types of strain that a tape undergoes when formed into a non-planar winding [17]. With this approach, a ruled surface describes the mid-surface of a tape conductor, and the different types of strain are calculated from the characteristics of the ruled surface and its base curve. This approach has for instance been used to design coil-end shapes for $\cos(n\theta)$ magnets [18], cloverleaf coils [19] and for stellarator coils [20]. The base curve can be described with Bézier splines for enhanced flexibility [21] or the edges of the tape can be described with non-uniform rational B-splines (NURBS) for computer-aided design integration [22].

A dedicated robotic winding cell for HTS coils has been implemented at KIT. The system serves both as a research platform for developing and validating robotic winding techniques, and as a practical tool for winding simpler experimental coils used in ongoing studies. Describing the winding shape as a ruled surface is particularly beneficial for robotic winding, as it allows the trajectory and rotations of the winding tool to be directly derived from the ruled surface.

This paper focuses on the design of a superellipse-shaped HTS coil with out-of-plane bending as a showcase for robotic winding of non-planar HTS coils. We employ the differential geometry approach to design the coil shape and adjust the shape to comply with the strain limitations of the HTS material. Representing the coil geometry analytically allows the relationships between the coil shape and the robot movements to be derived more easily than with a purely numerical design. The magnetic flux density generated by the coil is computed, and a suitable 3D-printed coil structure is produced. The winding tool trajectory and rotations are derived from the coil's shape-parameters. They are, together with the workpiece positioner rotation, implemented in a robot program. Figure 2 shows the robotic setup during a winding test performed to verify the robot program. The robotic system winds the coils without turn-to-turn insulation. The no-insulation coil is tested at 77 K in liquid nitrogen. We present winding results and electromagnetic measurements of the non-planar coil.

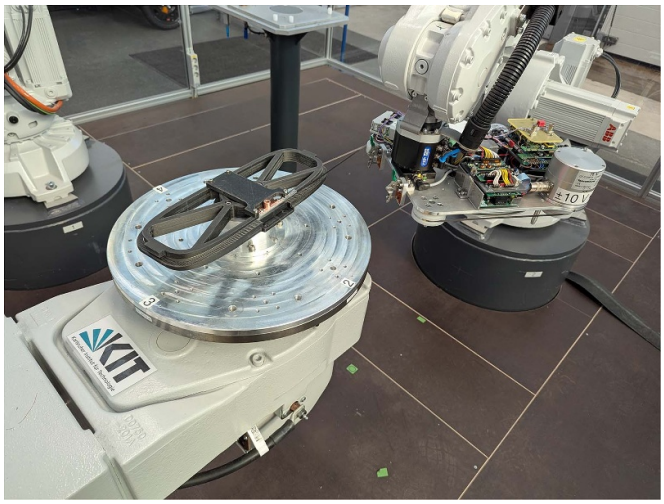

Figure 2. Winding test of the non-planar superellipse coil using the robotic setup.

2. Differential geometry approach to coil shape design

Differential geometry provides a powerful framework to describe and optimize the shape of coils in three-dimensional space. The symbols related to geometry are summarized in table A1.

2.1. Tape center curve

For a flat tape conductor, the center curve can be represented by a parameterized curve $\boldsymbol{\gamma} : (a,b) \to \mathbb{R}^3$ where $(a,b) = \{t \in \mathbb{R} \mid a < t < b\}$. Using the dot-notation for differentiation with respect to t, the first derivative $\dot{\boldsymbol{\gamma}}(t)$ of the curve is called the tangent vector of $\boldsymbol{\gamma}$ at the parameter value t. The norm of the tangent vector, which represents the speed of a point moving along the trajectory of $\boldsymbol{\gamma}$, is $\|\dot{\boldsymbol{\gamma}}\|$. A curve can be reparameterized to be unit-speed by using the arc-length of the curve as a new parameter. The arc-length of a curve $\boldsymbol{\gamma}$ starting at the point $\boldsymbol{\gamma}(t_0)$ is

$$s(t) = \int_{t_0}^{t} \|\dot{\boldsymbol{\gamma}}(u)\| \, \mathrm{d}u.$$

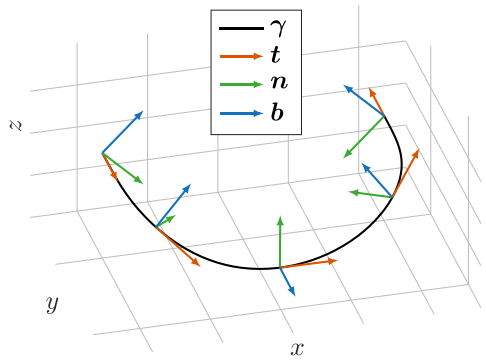

Figure 3. Example of a Frenet–Serret frame $\{\boldsymbol{t},\boldsymbol{n},\boldsymbol{b}\}$ moving along a space curve $\boldsymbol{\gamma}$.

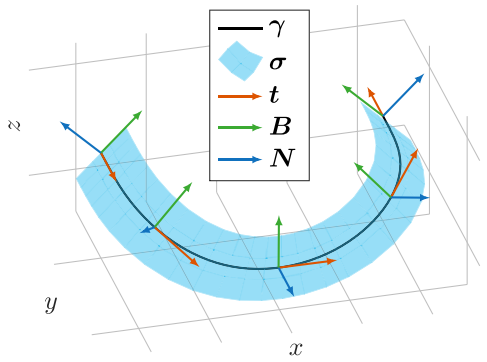

Figure 4. Illustration of a Darboux frame $\boldsymbol{t},\boldsymbol{B},\boldsymbol{N}$ evolving along a base curve $\boldsymbol{\gamma}$ on a ruled surface $\boldsymbol{\sigma}$. In this example, the ruling direction $\boldsymbol{\delta}$ is aligned with the intrinsic normal $\boldsymbol{B}$.

Many texts assume a unit-speed parameterization, which simplifies some formulas, however we avoid making this assumption. In a general parameterization, the *unit tangent vector* is given by

$$\boldsymbol{t} = \frac{\dot{\boldsymbol{\gamma}}}{\|\dot{\boldsymbol{\gamma}}\|}. \tag{1}$$

The *unit normal vector* can be computed from $\boldsymbol{t}$ by

$$\boldsymbol{n} = \frac{\dot{\boldsymbol{t}}}{\|\dot{\boldsymbol{t}}\|}. \tag{2}$$

The *unit binormal vector* is orthogonal to both $\boldsymbol{t}$ and $\boldsymbol{n}$, since

$$\boldsymbol{b} = \boldsymbol{t} \times \boldsymbol{n}.$$

The three vectors $\boldsymbol{t}(t)$, $\boldsymbol{n}(t)$, $\boldsymbol{b}(t)$ form an orthonormal basis called the *Frenet–Serret frame*. The Frenet–Serret formulas relate the derivatives of the basis vectors to the curvature κ and torsion τ of $\boldsymbol{\gamma}$,

$$\begin{bmatrix} \dot{\boldsymbol{t}} \\ \dot{\boldsymbol{n}} \\ \dot{\boldsymbol{b}} \end{bmatrix} = \|\dot{\boldsymbol{\gamma}}\| \begin{bmatrix} 0 & \kappa & 0 \\ -\kappa & 0 & \tau \\ 0 & -\tau & 0 \end{bmatrix} \begin{bmatrix} \boldsymbol{t} \\ \boldsymbol{n} \\ \boldsymbol{b} \end{bmatrix}. \tag{3}$$

The Frenet–Serret equations (3) show that the curvature κ quantifies the rate at which the Frenet–Serret frame rotates within the osculating plane spanned by $\boldsymbol{t}$ and $\boldsymbol{n}$. The torsion τ quantifies the rate at which the binormal vector $\boldsymbol{b}$, and thus the osculating plane itself, rotates about the tangent vector $\boldsymbol{t}$ as the frame progresses along the curve. Figure 3 shows an example of a Frenet–Serret frame moving along a curve $\boldsymbol{\gamma}$, where the frame evolves according to the local curvature and torsion. The curvature κ is non-negative and proportional to the rate of change of the tangent vector,

$$\kappa = \frac{\|\dot{\boldsymbol{t}}\|}{\|\dot{\boldsymbol{\gamma}}\|} = \frac{\|\ddot{\boldsymbol{\gamma}} \times \dot{\boldsymbol{\gamma}}\|}{\|\dot{\boldsymbol{\gamma}}\|^3}. \tag{4}$$

The torsion τ is a signed quantity proportional to the rate of change of the binormal vector and is given by [23]

$$\tau = \frac{(\dot{\boldsymbol{\gamma}} \times \ddot{\boldsymbol{\gamma}}) \cdot \dddot{\boldsymbol{\gamma}}}{\|\dot{\boldsymbol{\gamma}} \times \ddot{\boldsymbol{\gamma}}\|^2}. \tag{5}$$

2.2. Tape mid-surface

While $\boldsymbol{\gamma}$ represents the center curve of the tape, the mid-surface of the tape is represented by a parameterized ruled surface $\boldsymbol{\sigma} : U \to \mathbb{R}^3$ where $U = \{(t,v) \in \mathbb{R}^2 \mid a < t < b\}$:

$$\boldsymbol{\sigma}(t,v) = \boldsymbol{\gamma}(t) + v\boldsymbol{\delta}(t). \tag{6}$$

Here, $\boldsymbol{\gamma}$ is called the *base curve* and $\boldsymbol{\delta}$ the *ruling direction*.

To describe the local geometry of the surface $\boldsymbol{\sigma}$ along the base curve $\boldsymbol{\gamma}$, we introduce an orthonormal frame $\{\boldsymbol{t},\boldsymbol{B},\boldsymbol{N}\}$, known as the *Darboux frame*. Here, $\boldsymbol{t}$ is the unit tangent vector of $\boldsymbol{\gamma}$ given by (1). Let $\boldsymbol{\sigma}_t = \|\dot{\boldsymbol{\gamma}}\|\boldsymbol{t} + v\dot{\boldsymbol{\delta}}$ and $\boldsymbol{\sigma}_v = \boldsymbol{\delta}$ denote the partial derivatives of $\boldsymbol{\sigma}(t,v)$ with respect to t and v, respectively. Then the *surface normal* to $\boldsymbol{\sigma}$ along the base curve $\boldsymbol{\gamma}(t)$ is

$$\boldsymbol{N}(t) = \frac{\boldsymbol{\sigma}_t(t,0) \times \boldsymbol{\sigma}_v(t,0)}{\|\boldsymbol{\sigma}_t(t,0) \times \boldsymbol{\sigma}_v(t,0)\|} = \frac{\boldsymbol{t}(t) \times \boldsymbol{\delta}(t)}{\|\boldsymbol{t}(t) \times \boldsymbol{\delta}(t)\|}. \tag{7}$$

The *intrinsic normal* $\boldsymbol{B}$ lies in the surface tangent plane and is orthogonal to both $\boldsymbol{N}$ and $\boldsymbol{t}$. It is defined as

$$\boldsymbol{B} = \boldsymbol{N} \times \boldsymbol{t}. \tag{8}$$

Figure 4 shows the Darboux frame along the curve $\boldsymbol{\gamma}$ lying on a ruled surface $\boldsymbol{\sigma}$. This is the same curve shown with its Frenet–Serret frame in figure 3. In general, the Frenet–Serret and Darboux frames are not aligned, as demonstrated in this example.

The Darboux derivative formulas describe how the frame vectors $\boldsymbol{t}$, $\boldsymbol{B}$, $\boldsymbol{N}$ evolve along the base curve $\boldsymbol{\gamma}$,

$$\begin{bmatrix} \dot{\boldsymbol{t}} \\ \dot{\boldsymbol{B}} \\ \dot{\boldsymbol{N}} \end{bmatrix} = \|\dot{\boldsymbol{\gamma}}\| \begin{bmatrix} 0 & \kappa_g & \kappa_n \\ -\kappa_g & 0 & \tau_g \\ -\kappa_n & -\tau_g & 0 \end{bmatrix} \begin{bmatrix} \boldsymbol{t} \\ \boldsymbol{B} \\ \boldsymbol{N} \end{bmatrix}. \tag{9}$$

These equations introduce three geometric quantities κ_n, κ_g, and τ_g, which characterize the local shape of a curve $\boldsymbol{\gamma}$ in a surface $\boldsymbol{\sigma}$. The *normal curvature* κ_n measures the bending of the curve in the direction of the surface normal:

$$\kappa_n = \frac{\ddot{\boldsymbol{\gamma}} \cdot \boldsymbol{N}}{\|\dot{\boldsymbol{\gamma}}\|^2}. \tag{10}$$

The *geodesic curvature* κ_g measures the bending of the curve in the direction of the intrinsic normal:

$$\kappa_g = \frac{\ddot{\boldsymbol{\gamma}} \cdot \boldsymbol{B}}{\|\dot{\boldsymbol{\gamma}}\|^2}. \tag{11}$$

The *geodesic torsion* τ_g measures the rotation of the surface normal $\boldsymbol{N}$ about the tangent direction:

$$\tau_g = \frac{\dot{\boldsymbol{\gamma}} \cdot \left(\boldsymbol{N} \times \dot{\boldsymbol{N}}\right)}{\|\dot{\boldsymbol{\gamma}}\|^2}. \tag{12}$$

The geodesic torsion can according to Bonnet's formula also be written as

$$\tau_g = \tau + \frac{\dot{\theta}}{\|\dot{\boldsymbol{\gamma}}\|}, \tag{13}$$

where θ is the angle between the normal vector $\boldsymbol{N}$ of the surface and the normal vector $\boldsymbol{n}$ of the base curve, i.e. $\cos\theta = \boldsymbol{N} \cdot \boldsymbol{n}$ [24]. We shall refer to the second term in (13) as the *twist rate* τ_t and compute it by

$$\tau_t = \tau_g - \tau. \tag{14}$$

The normal and geodesic curvatures are related to the total curvature by $\kappa^2 = \kappa_n^2 + \kappa_g^2$. These two curvatures, along with the two terms making up the geodesic torsion, contribute to intrinsic strain within of the tape. The normal curvature κ_n and the torsion τ contribute to normal strain ε_n, the geodesic curvature κ_g contributes to geodesic strain ε_g, and the twist rate τ_t contributes to twisting strain ε_t.

2.3. Developable surfaces

The Gaussian curvature of a ruled surface is

$$K = \frac{-\left(\dot{\boldsymbol{\delta}} \cdot \boldsymbol{N}\right)^2}{\|\boldsymbol{\sigma}_t \times \boldsymbol{\sigma}_v\|^2}. \tag{15}$$

A surface with zero Gaussian curvature is called a *developable surface*. Developable surfaces are locally isometric to the plane, meaning they can be constructed by smoothly bending flat sheets without in-plane deformation, making them suitable for shaping HTS tapes while minimizing mechanical strain [25]. Coil shapes where the tape's mid-surface is developable can be constructed by choosing the ruling direction $\boldsymbol{\delta}$ to be parallel to the Darboux vector $\boldsymbol{\omega} = \tau\boldsymbol{t} + \kappa\boldsymbol{b}$. Since $\boldsymbol{\omega}$ always lies in the rectifying plane spanned by $\boldsymbol{t}$ and $\boldsymbol{b}$, the resulting developable surface is called the *rectifying developable* of the base curve $\boldsymbol{\gamma}$ [26]. For this choice of ruling direction, the surface normal is $\boldsymbol{N} = -\boldsymbol{n}$ and the intrinsic normal is $\boldsymbol{B} = \boldsymbol{b}$ along $\boldsymbol{\gamma}$. The constant angle between $\boldsymbol{N}$ and $\boldsymbol{n}$ implies a vanishing twist rate, $\tau_t = 0$.

For the ruled surface in (6), the *striction curve* $\boldsymbol{\Gamma}$ is the locus of points for which the derivative of the ruling direction $\boldsymbol{\delta}$ is perpendicular to the surface, i.e. where $\dot{\boldsymbol{\delta}} \cdot \boldsymbol{\sigma}_t = 0$ and $\dot{\boldsymbol{\delta}} \cdot \boldsymbol{\sigma}_v = 0$. Hence, the striction curve is given by $\boldsymbol{\Gamma}(t) = \boldsymbol{\sigma}(t, v(t))$ where

$$v(t) = -\frac{\dot{\boldsymbol{\gamma}}(t) \cdot \dot{\boldsymbol{\delta}}(t)}{\|\dot{\boldsymbol{\delta}}(t)\|^2}.$$

A developable surface can have one of the following three types of singularities at its striction curve: cuspidal edge, swallowtail, or cuspidal cross-cap [27]. When such a singularity lies within the tape's width, the surface is no longer smooth within the region of interest and fails to represent a physical tape. The shape of the base curve must then be adjusted to move the striction curve further away from the base curve. Hence, not every coil shape can be created from a developable surface. Additionally, the magnetic field generated by a coil shaped as a developable surface might no longer be predominantly parallel to the HTS plane, resulting in lower HTS performance [28]. In such cases, it may be more advantageous to consider a coil shape defined by a non-developable ruled surface, which avoids singularities and more effectively accommodates the field configuration.

3. Mechanical strain

This section considers only the intrinsic strain resulting from the coil geometry. Strain caused by the winding process, cooldown, or operation are not included. The symbols related to mechanics are summarized in table A2.

Engineering strain is defined as

$$\varepsilon = \frac{l - l_0}{l_0},$$

where l is the length after deformation and l_0 is the length before deformation. By adding a constant distance λ to the mid-surface $\boldsymbol{\sigma}$ of the HTS tape, we can describe the HTS layer as the family of curves

$$\boldsymbol{\alpha}(t; v) = \boldsymbol{\sigma}(t, v) - \lambda \boldsymbol{N}(t)$$

with $v \in [-w/2, w/2]$ and $t \in [0, t_0]$. The length of $\boldsymbol{\alpha}$ is the length after deformation,

$$l = \int_0^{t_0} \|\dot{\boldsymbol{\alpha}}\| \, \mathrm{d}t.$$

The length of the base curve $\boldsymbol{\gamma}$ is unchanged after deformation of $\boldsymbol{\sigma}$, so the length of $\boldsymbol{\alpha}$ before deformation is equal to the length of $\boldsymbol{\gamma}$ after deformation,

$$l_0 = \int_0^{t_0} \|\dot{\boldsymbol{\gamma}}\| \, \mathrm{d}t.$$

Assuming that the HTS layer is located on the inside of the bending direction, the engineering normal strain is entirely compressive within the HTS layer and given by

$$\varepsilon_{\mathrm{n}}(t) = \sqrt{(1 \pm \lambda\kappa_{\mathrm{n}}(t))^2 + (\lambda\tau(t))^2} - 1. \tag{16}$$

The geodesic bending causes a strain within the HTS layer, where half of the HTS layer is in compression and the other half experiences tensile strain. The geodesic strain of the HTS layer is given by

$$\varepsilon_{\mathrm{g}}(t,v) = \mp v\kappa_{\mathrm{g}}(t). \tag{17}$$

The signs of κ_{n}, and κ_{g} depend on the parameterization of $\boldsymbol{\gamma}$, so their signs in (16) and (17) should be chosen such that ε_{n} and ε_{g} are negative where the curves are compressed and positive where the curves are elongated. The twisting strain is entirely tensile within the HTS layer and given by

$$\varepsilon_{\mathrm{t}}(t,v) = \sqrt{1 + (v^2 + \lambda^2)[\tau_{\mathrm{t}}(t)]^2} - 1. \tag{18}$$

The derivation of the strain expressions are found in in appendix B. Each type of strain is in the longitudinal direction of the HTS tape. Hence, the total intrinsic strain within the HTS layer is simply the sum of them

$$\varepsilon_{\mathrm{i}}(t,v) = \varepsilon_{\mathrm{n}}(t) + \varepsilon_{\mathrm{g}}(t,v) + \varepsilon_{\mathrm{t}}(t,v), \tag{19}$$

with $v \in [-w/2, w/2]$.

4. Non-planar superellipse coil shape design

This section applies the differential geometry approach to designing the shape of a non-planar superellipse HTS coil. A base curve $\boldsymbol{\gamma}$ lying within a surface $\boldsymbol{\eta}(x,y) = (x,y,h(x,y))^{\mathsf{T}}$ describes the center curve of a winding turn. The normal vector $\boldsymbol{\delta}$ of $\boldsymbol{\eta}$ constitutes the direction vector of a ruled surface representing the mid-surface of the HTS tape. Table 1 lists the shape parameters for the non-planar superellipse HTS coil.

4.1. Base curve

A *superellipse* is a generalization of an ellipse and is in the xy-plane defined as

$$x(t) = r(t)\cos t, \tag{20}$$
$$y(t) = r(t)\sin t. \tag{21}$$

The radial function $r : \mathbb{R} \to \mathbb{R}^+$ is given by

$$r(t) = \left(\frac{|\cos t|^m}{a^m} + \frac{|\sin t|^m}{b^m} \right)^{-1/m}, \tag{22}$$

where $a, b > 0$ are the semi-axes, and $n > 0$ is the shape exponent [29]. For $n < 2$, the curve is a hypoellipse; for $n = 2$, an ordinary ellipse; and for $n > 2$, a hyperellipse. To ensure smoothness at every point, we assume $n \geqslant 2$ for coil design. By adjusting its shape parameters, the superellipse smoothly transitions between circular, elliptical, and rounded rectangular forms, providing great flexibility in coil shape design. It also avoids points of zero curvature, where the Frenet–Serret frame is undefined, allowing the approach described in section 2 to be applied directly without modification.

Table 1. Shape parameters for the non-planar superellipse coil.

Symbol	Description	Value	Unit
a	Semi-major axis	180	mm
b	Semi-minor axis	60	mm
m	Shape exponent	4	—
κ_{g0}	Central geodesic curvature	0.5	m^{-1}
w	Tape width	4	mm
d	Substrate thickness	50	µm

To construct a non-planar version of the curve, we introduce a height function $h : \mathbb{R}^2 \to \mathbb{R}$ describing the deviation from the xy-plane. We let h define a surface $\boldsymbol{\eta} : \mathbb{R}^2 \to \mathbb{R}^3$ by

$$\boldsymbol{\eta}(x,y) = (x,y,h(x,y))^{\mathsf{T}}. \tag{23}$$

We now define a *non-planar superellipse* as a 2π-periodic curve $\boldsymbol{\gamma} : \mathbb{R} \to \mathbb{R}^3$, obtained by mapping a planar superellipse onto the surface $\boldsymbol{\eta}$,

$$\boldsymbol{\gamma}(t) = (x(t), y(t), z(t))^{\mathsf{T}}, \tag{24}$$

where x and y are given by (20) and (21), respectively, and

$$z(t) = h(x(t), y(t)).$$

While the planar superellipse remains in the xy-plane, $\boldsymbol{\gamma}(t) \in \boldsymbol{\eta}$ for all $t \in \mathbb{R}$. This allows us to control the out-of-plane deformation by choosing a suitable function $h(x,y)$. For generality, we shall express all equations using an arbitrary function $h(x,y)$. However, for the coil we constructed, we used a parabolic bending given by

$$h(x,y) = \frac{1}{2}\kappa_{\mathrm{g0}}x^2, \tag{25}$$

where κ_{g0} is the curvature of the out-of-plane bending at $x = 0$.

4.2. Unit tangent vector

The tangent vector to $\boldsymbol{\gamma}$ is given by

$$\dot{\boldsymbol{\gamma}}(t) = (\dot{x}(t), \dot{y}(t), \dot{z}(t))^{\mathsf{T}}, \tag{26}$$

where

$$\dot{x}(t) = \dot{r}(t)\cos t - r(t)\sin t,$$
$$\dot{y}(t) = \dot{r}(t)\sin t + r(t)\cos t,$$
$$\dot{z}(t) = \dot{x}(t)\,h_x(x,y) + \dot{y}(t)\,h_y(x,y),$$

where $h_x = \frac{\partial h}{\partial x}$ and $h_y = \frac{\partial h}{\partial y}$ are the partial derivatives of $h(x,y)$. The derivative of the radial function r is

$$\dot{r}(t) = r^{m+1}(t)\cos t \sin t \left(\frac{|\cos t|^{m-2}}{a^m} - \frac{|\sin t|^{m-2}}{b^m} \right).$$

The speed of $\boldsymbol{\gamma}$ is

$$\|\dot{\boldsymbol{\gamma}}\| = \sqrt{r^2 + \dot{r}^2 + (\dot{x}h_x + \dot{y}h_y)^2}. \tag{27}$$

Since $r > 0$, the speed is always strictly positive, i.e. $\|\dot{\boldsymbol{\gamma}}(t)\| > 0$ for all $t \in \mathbb{R}$, implying that the curve $\boldsymbol{\gamma}$ is regular. The unit tangent vector to $\boldsymbol{\gamma}$ is calculated by inserting the expressions (26) for $\dot{\boldsymbol{\gamma}}$ and (27) for $\|\dot{\boldsymbol{\gamma}}\|$ into the expression (1) for $\boldsymbol{t}$. The unit tangent vector will be used to define the robotic winding tool trajectory.

4.3. Acceleration vector

The second derivative vector, which represents the acceleration of a point moving along the trajectory of $\boldsymbol{\gamma}$, is given by

$$\ddot{\boldsymbol{\gamma}}(t) = (\ddot{x}(t), \ddot{y}(t), \ddot{z}(t))^{\mathsf{T}}, \tag{28}$$

where

$$\begin{aligned}
\ddot{x}(t) &= \ddot{r}\cos t - 2\dot{r}\sin t - r\cos t, \\
\ddot{y}(t) &= \ddot{r}\sin t + 2\dot{r}\cos t - r\sin t, \\
\ddot{z}(t) &= \dot{x}^2 h_{xx}(x,y) + \ddot{x}h_x(x,y) + \dot{y}^2 h_{yy}(x,y) \\
&\quad + \ddot{y}h_y(x,y) + 2\dot{x}\dot{y}h_{xy}(x,y),
\end{aligned}$$

where $h_{xx} = \frac{\partial^2 h}{\partial x^2}$, $h_{yy} = \frac{\partial^2 h}{\partial y^2}$, and $h_{xy} = \frac{\partial^2 h}{\partial y \partial x}$ are the second-order partial derivatives of the function $h(x,y)$, and the second derivative of the radial function r is

$$\begin{aligned}
\ddot{r}(t) &= (m+1)\, r^{-1}\dot{r}^2 \\
&\quad + r^{m+1}\left(\cos^2 t - \sin^2 t\right)\left(\frac{|\cos t|^{m-2}}{a^m} - \frac{|\sin t|^{m-2}}{b^m} \right) \\
&\quad - (m-2)\, r^{m+1}\left(\frac{\sin^2 t |\cos t|^{m-2}}{a^m} + \frac{\cos^2 t |\sin t|^{m-2}}{b^m} \right).
\end{aligned}$$

The acceleration vector (28) is used to compute the normal and geodesic curvatures of $\boldsymbol{\gamma}$ on $\boldsymbol{\sigma}$.

4.4. Unit normal vector

The derivative of the unit tangent vector $\boldsymbol{t}$ is

$$\dot{\boldsymbol{t}} = \frac{\|\dot{\boldsymbol{\gamma}}\|^2 \ddot{\boldsymbol{\gamma}} - (\dot{\boldsymbol{\gamma}} \cdot \ddot{\boldsymbol{\gamma}})\dot{\boldsymbol{\gamma}}}{\|\dot{\boldsymbol{\gamma}}\|^3} \tag{29}$$

and the norm of $\dot{\boldsymbol{t}}$ is

$$\|\dot{\boldsymbol{t}}\| = \frac{\|\ddot{\boldsymbol{\gamma}} \times \dot{\boldsymbol{\gamma}}\|}{\|\dot{\boldsymbol{\gamma}}\|^2}. \tag{30}$$

The normal vector $\boldsymbol{n}$ for $\boldsymbol{\gamma}$ is calculated by inserting the expressions (29) for $\dot{\boldsymbol{t}}$ and (30) for $\|\dot{\boldsymbol{t}}\|$ into the expression (2).

4.5. Curvature and torsion

The curvature κ is calculated from (4). The third derivative of $\boldsymbol{\gamma}$ is

$$\dddot{\boldsymbol{\gamma}}(t) = (\dddot{x}(t), \dddot{y}(t), \dddot{z}(t))^{\mathsf{T}}, \tag{31}$$

where

$$\begin{aligned}
\dddot{x}(t) &= (\dddot{r} - 3\dot{r})\cos t + (r - 3\ddot{r})\sin t, \\
\dddot{y}(t) &= (\dddot{r} - 3\dot{r})\sin t - (r - 3\ddot{r})\cos t \\
\dddot{z}(t) &= h_{xxx}(x,y)\dot{x}^3 + 3h_{xxy}(x,y)\dot{x}^2\dot{y} \\
&\quad + 3h_{xyy}(x,y)\dot{x}\dot{y}^2 + h_{yyy}(x,y)\dot{y}^3 \\
&\quad + 3h_{xx}(x,y)\dot{x}\ddot{x} + 3h_{xy}(x,y)(\dot{x}\ddot{y} + \dot{y}\ddot{x}) \\
&\quad + 3h_{yy}(x,y)\dot{y}\ddot{y} + h_x(x,y)\dddot{x} + h_y(x,y)\dddot{y}.
\end{aligned}$$

Here $h_{xxx} = \frac{\partial^3 h}{\partial x^3}$, $h_{xxy} = \frac{\partial^3 h}{\partial y \partial x^2}$, $h_{xyy} = \frac{\partial^3 h}{\partial y^2 \partial x}$, and $h_{yyy} = \frac{\partial^3 h}{\partial y^3}$ are the third-order partial derivatives of the function $h(x,y)$, and the third derivative of the radial function r is

$$\begin{aligned}
\dddot{r}(t) &= -(m+1)\, r^{-2}\dot{r}^3 + 2(m+1)\, r^{-1}\dot{r}\ddot{r} \\
&\quad + (m+1)\, r^m \dot{r}\left(\cos^2 t - \sin^2 t\right) \\
&\quad \times \left(\frac{|\cos t|^{m-2}}{a^m} - \frac{|\sin t|^{m-2}}{b^m} \right) \\
&\quad - 4r^{m+1}\sin t \cos t \left(\frac{|\cos t|^{m-2}}{a^m} - \frac{|\sin t|^{m-2}}{b^m} \right) \\
&\quad - (m-2)\, r^{m+1}\left(\cos^2 t - \sin^2 t\right)\sin t \cos t \\
&\quad \times \left(\frac{|\cos t|^{m-4}}{a^m} + \frac{|\sin t|^{m-4}}{b^m} \right) \\
&\quad - (m-2)(m+1)\, r^m \dot{r} \\
&\quad \times \left(\frac{\sin^2 t |\cos t|^{m-2}}{a^m} + \frac{\cos^2 t |\sin t|^{m-2}}{b^m} \right) \\
&\quad - (m-2)\, r^{m+1}\sin t \cos t \\
&\quad \times \left(\frac{2|\cos t|^{m-2} - (m-2)\sin^2 t |\cos t|^{m-4}}{a^m} \right. \\
&\quad \left. - \frac{2|\sin t|^{m-2} - (m-2)\cos^2 t |\sin t|^{m-4}}{b^m} \right).
\end{aligned}$$

The torsion τ is computed by inserting the expressions (26) for $\dot{\boldsymbol{\gamma}}$, (28) for $\ddot{\boldsymbol{\gamma}}$, and (31) for $\dddot{\boldsymbol{\gamma}}$ into the expression (5). Both the curvature and torsion are π-periodic. Figure 5 shows κ and τ as functions of t when h is given by (25). The curvature reaches its maximum at the corners of the superellipse, while the torsion is greatest where z changes most rapidly.

4.6. Normal to bending surface

Let $\boldsymbol{\eta}_x$ and $\boldsymbol{\eta}_y$ denote the partial derivatives of $\boldsymbol{\eta}$. Then the unit normal $\boldsymbol{\delta}$ to $\boldsymbol{\eta}$ is

$$\boldsymbol{\delta} = \frac{\boldsymbol{\eta}_x \times \boldsymbol{\eta}_y}{\|\boldsymbol{\eta}_x \times \boldsymbol{\eta}_y\|} = \frac{(-h_x, -h_y, 1)^{\mathsf{T}}}{\sqrt{1 + h_x^2 + h_y^2}}. \tag{32}$$

This normal vector will be used to define the rulings of the surface representing the mid-surface of the HTS tape. This ruling

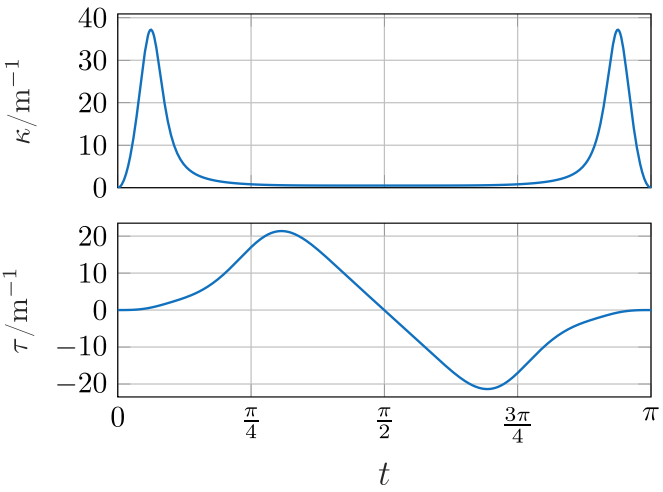

Figure 5. The π-periodic curvature κ and torsion τ of $\boldsymbol{\gamma}$ as functions of t for h given by (25).

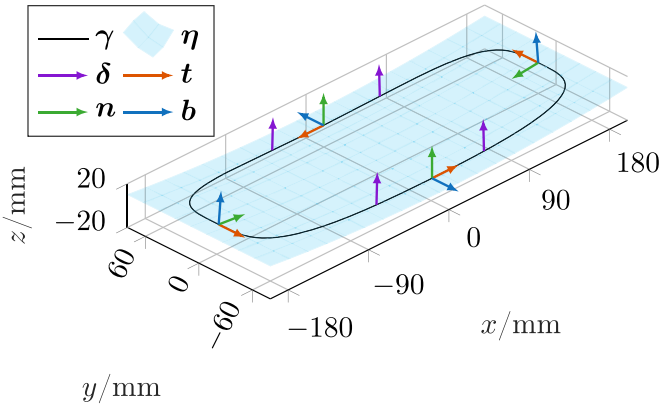

Figure 6. The base curve $\boldsymbol{\gamma}$ in the surface $\boldsymbol{\eta}$ representing the bending of the coil together with the surface normal $\boldsymbol{\eta}$. The vectors of the Frenet–Serret frame $\{\boldsymbol{t},\boldsymbol{n},\boldsymbol{b}\}$ are shown along the base curve.

direction is orthogonal to the $\dot{\boldsymbol{\gamma}}$, i.e. $\boldsymbol{\delta}\cdot\dot{\boldsymbol{\gamma}}=0$. Figure 6 shows $\boldsymbol{\gamma}$ in the surface $\boldsymbol{\eta}$ together with the surface normal vector $\boldsymbol{\delta}$ and the vectors of the Frenet–Serret frame $\{\boldsymbol{t},\boldsymbol{n},\boldsymbol{b}\}$.

4.7. Ruled surface

We describe the mid-surface of the HTS tape as a ruled surface $\boldsymbol{\sigma}$ as in (6). The base curve $\boldsymbol{\gamma}$ is given by (24) and the ruling direction $\boldsymbol{\delta}$ is given by (32). Since $\boldsymbol{\delta}$ is unit-length and orthogonal to $\dot{\boldsymbol{\gamma}}$, we have $\|\boldsymbol{\delta}\times\dot{\boldsymbol{\gamma}}\|=\|\dot{\boldsymbol{\gamma}}\|$ and the expression for the surface normal $\boldsymbol{N}$ given by (7) reduces to

$$\boldsymbol{N}=\boldsymbol{t}\times\boldsymbol{\delta}. \tag{33}$$

The intrinsic normal given by (8) is

$$\boldsymbol{B}=\boldsymbol{\delta}. \tag{34}$$

Figure 7 shows the ruled surface $\boldsymbol{\sigma}$ and the vectors of the Darboux frame $\{\boldsymbol{t},\boldsymbol{B},\boldsymbol{N}\}$. Figure 8 shows the normal curvature κ_n, geodesic curvature κ_g, geodesic torsion τ_g and twist rate τ_t for $\boldsymbol{\gamma}$ in the surface $\boldsymbol{\sigma}$ computed with (10)–(12) and (14)

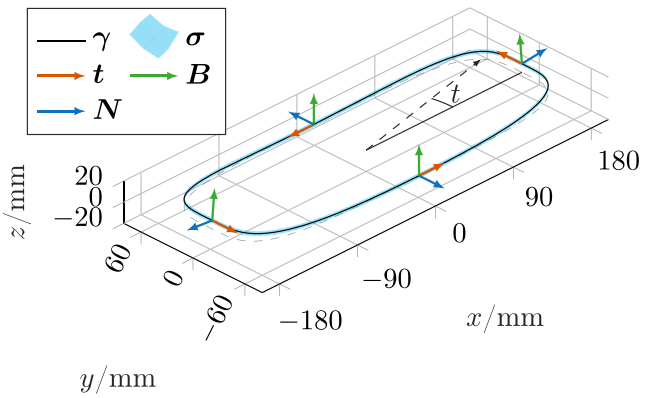

Figure 7. The base curve $\boldsymbol{\gamma}$ and the ruled surface $\boldsymbol{\sigma}$ representing the mid-surface of the innermost winding turn of the non-planar superellipse coil. The vectors of the Darboux frame $\{\boldsymbol{t},\boldsymbol{B},\boldsymbol{N}\}$ are shown along the base curve.

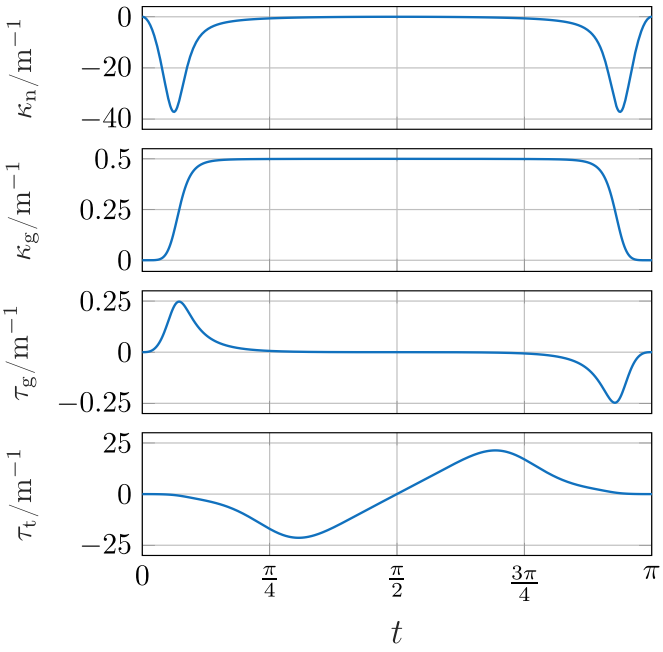

Figure 8. The π-periodic normal curvature κ_n, geodesic curvature κ_g, geodesic torsion τ_g, and twist rate τ_t of $\boldsymbol{\gamma}$ in σ as functions of t.

for h given by (25) and the shape parameters listed in table 1. The normal curvature κ_n reflects that easy-way bending is concentrated at the corners of the superellipse, while the geodesic curvature κ_g captures the hard-way bending distributed along the major axis. Although the unit normal $\boldsymbol{n}$ rotates about the tangent $\boldsymbol{t}$ along the base curve $\boldsymbol{\gamma}$, the surface normal $\boldsymbol{N}$ remains nearly fixed relative to $\boldsymbol{t}$. Consequently, the geodesic torsion τ_g is small, and the twist rate τ_t closely follows the negative of the torsion τ, in accordance with (14).

4.8. Intrinsic strain

Figure 9 shows the strain contributions from normal bending (16), geodesic bending (17) and twisting (18), together

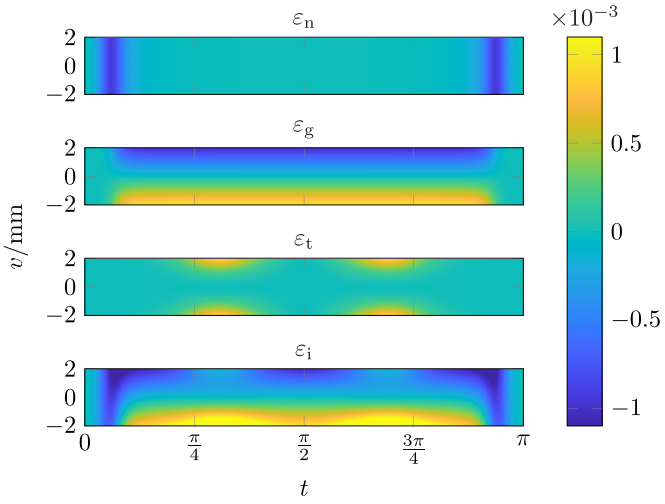

Figure 9. Normal strain ε_n, geodesic strain ε_g, and torsional strain ε_t in the tv-plane for the non-planar superellipse coil. The minimum and maximum strain values are listed in table 2.

Table 2. The minimum and maximum strain values.

Symbol	Description	Value	Unit
$\varepsilon_{n,min}$	Minimum normal strain	-0.93×10^{-3}	—
$\varepsilon_{n,max}$	Maximum normal strain	0	—
$\varepsilon_{g,min}$	Minimum geodesic strain	-1.00×10^{-3}	—
$\varepsilon_{g,max}$	Maximum geodesic strain	1.00×10^{-3}	—
$\varepsilon_{t,min}$	Minimum twisting strain	0	—
$\varepsilon_{t,max}$	Maximum twisting strain	0.91×10^{-3}	—
$\varepsilon_{i,min}$	Minimum intrinsic strain	-1.32×10^{-3}	—
$\varepsilon_{i,max}$	Maximum intrinsic strain	1.90×10^{-3}	—
ε_{min}	Compressive strain limit	-8×10^{-3}	—
ε_{max}	Tensile strain limit	5×10^{-3}	—

with the total intrinsic strain (19). The strain values are computed for the HTS layer located at half the substrate thickness from the mid-surface, $\lambda = d/2$. The maximum intrinsic strain within the HTS layer is obtained when $v = -w/2$. The minimum and maximum strain values are listed in table 2.

The irreversible compressive strain limit for HTS tapes is about $\varepsilon_{min} = -8 \times 10^{-3}$ while the irreversible tensile strain limit is about $\varepsilon_{max} = 5 \times 10^{-3}$ [30]. However, besides the intrinsic strain, the HTS layer also experiences winding strain, thermal strain, and Lorentz force-induced strain. For this non-planar superellipse coil we allocate a maximum of 2×10^{-3} for intrinsic strain ε_i.

5. Robotic winding

The KIT robotic winding cell contains three ABB industrial robots. The robots are programmed in RAPID using RobotStudio. To program the robot movement, the winding tool trajectory and the rotation angles about the z-axis, y-axis and x-axis must be calculated together with the rotation angle of the workpiece positioner.

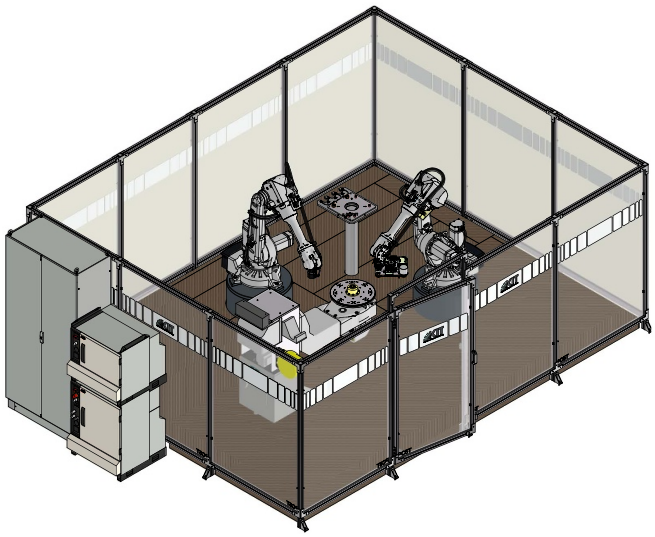

Figure 10. The KIT robotic winding cell contains one IRBP A-500 industrial robot positioner and two IRB 2600-20/1.65 articulated industrial robots.

5.1. Robotic winding setup

Robotic winding offers several advantages to conventional winding machines. Robots are easily adaptable to different winding patterns, and their movement is easily repeatable, giving reproducible winding results. Additionally, the same winding techniques can be applied with larger robots to wind larger coils. The KIT winding cell shown in figure 10 features transparent walls and a door with a locking system for operator safety. The ABB robotic system consists of one IRBP A-500 industrial robot positioner and two IRB 2600-20/1.65 articulated industrial robots. Each articulated robot is equipped with a STC20-4E Swivel Tool Changer at the wrist. A tool stand stores the currently unused robot tools and the articulated robots can pick up their tools from there. All three robots are placed within reach of each other, allowing the two articulated robots to exchange the winding tool between them.

5.2. Winding tool

The articulated robots use the internally developed winding tool with tension control shown in figure 11. During the winding process, the HTS tape is released from the spool with a specified tension. The winding tool is constructed on an aluminum base plate. The spool of HTS tape is mounted to a rotary actuator from the bottom of the base plate. Deflection rollers lead the tape from the spool towards the coil. On the top of the base plate are, in addition to the rotary actuator, mounted two tool attachment units and electronics for tension control.

Figure 12 shows a signal flow diagram for the winding tool electronics which includes all the winding tool components listed in table 3. The winding tension is maintained via a closed-loop feedback system. A target tension is specified by the user via a human machine interface (HMI) panel and

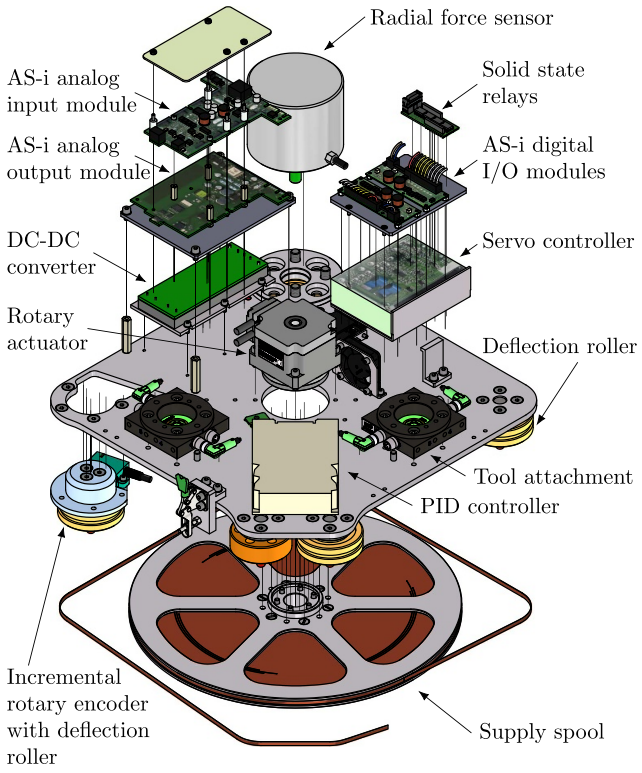

Figure 11. Exploded view of the winding tool.

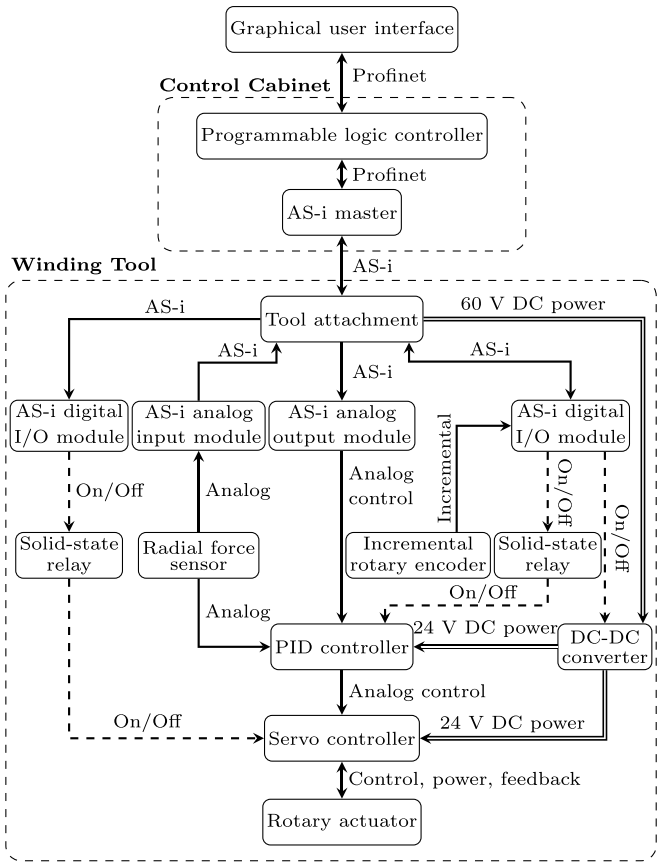

Figure 12. Signal flow diagram for the winding tool electronics.

transmitted through the programmable logic controller (PLC) over the AS-interface (AS-i) network to the PID controller. The radial force sensor continuously measures the actual tension in the HTS tape and sends this data to both the PLC and the PID controller. The PID controller compares the measured tension to the setpoint and generates a control signal. This signal is sent to the servo controller, which regulates the rotary actuator driving the supply spool, maintaining the desired tension in real time. An incremental rotary encoder measures the rotation of the supply spool and transmits the signal to the PLC via the AS-i network. This data is used to calculate the length of HTS tape released, displayed on the HMI panel. Additional support electronics include solid-state relays for enabling power to control components and a DC-DC converter to supply 24 V power from a 60 V DC supply line. All components are coordinated through the AS-i network, allowing integrated analog and digital control signals to be exchanged between the winding tool and control cabinet.

Table 3. Winding tool components.

Component	Description
Graphical user interface	SIMATIC HMI panel
PLC	SIMATIC S7-1500 PLC
AS-i master	IFM AS-i Gateway AC1401
Tool attachment	RSP Tool attachment (TA20-4E)
AS-i digital I/O module	IFM AC2750
AS-i analog input module	Siemens 3RK1207-0CE00-2AA2
AS-i analog output module	Siemens 3RK1107-0BE00-2AA2
Solid-state relay	Panasonic AQW215
Radial force sensor	Tensometric CF-COMP-PRO
Incremental rotary encoder	P&F MNI20N
PID controller	universal PID Controller BM 104
DC-DC Converter	Vicor VI-243-EW
Servo controller	Harmonic Drive HA-680
Rotary actuator	Harmonic Drive FHA-C Mini

5.3. Robot programming

The robots are programmed in RAPID, which is a high-level programming language used to control ABB industrial robots. A digital twin of the robot station has been set up in RobotStudio. Using RobotStudio, the robot programs can be prepared and simulated on the robot's digital twins [31]. Moving the articulated robots along a trajectory requires either a full list of coordinate points along that trajectory or the points can be computed from equations. Rotation of the winding tool requires specification of the angle by which the tool should be rotated about each coordinate axis in the following order: rotation about the z-axis, rotation about the y-axis, and rotation about the x-axis.

5.3.1. Winding tool trajectory. The robotic winding tool should move at a fixed distance ℓ to the inner coil shape. The tape should be added to the coil tangentially from the winding tool. Hence, the flat winding path can be described by

$$\boldsymbol{\beta}(t) = \boldsymbol{\gamma}(t) + \ell \boldsymbol{t}(t)\,. \tag{35}$$

The instantaneous direction of the winding tool movement is tangent to $\boldsymbol{\beta}$,

$$\dot{\boldsymbol{\beta}} = \dot{\boldsymbol{\gamma}} + \ell\dot{\boldsymbol{t}} = \|\dot{\boldsymbol{\gamma}}\|\,(\boldsymbol{t} + \ell\kappa\boldsymbol{n})\,,$$

where we have used the tangential equation of the Frenet–Serret frame (3).

5.3.2. Tool rotation about each axis. The winding tool must, at each point along its trajectory, be oriented according to the basis vectors of the Darboux frame at the current winding point $\boldsymbol{\gamma}(t)$. Coordinate rotations $\boldsymbol{R}_i : \mathbb{R} \to \mathrm{SO}(3)$, $i \in \{x, y, z\}$ by an angle θ about the x-, y- and z-axes are

$$\boldsymbol{R}_x(\theta) = \begin{bmatrix} 1 & 0 & 0 \\ 0 & \cos\theta & -\sin\theta \\ 0 & \sin\theta & \cos\theta \end{bmatrix},$$

$$\boldsymbol{R}_y(\theta) = \begin{bmatrix} \cos\theta & 0 & \sin\theta \\ 0 & 1 & 0 \\ -\sin\theta & 0 & \cos\theta \end{bmatrix},$$

$$\boldsymbol{R}_z(\theta) = \begin{bmatrix} \cos\theta & -\sin\theta & 0 \\ \sin\theta & \cos\theta & 0 \\ 0 & 0 & 1 \end{bmatrix}.$$

The Tait–Bryan angle sequence with rotations applied successively about the rotated z, y, and x-axes is

$$\boldsymbol{R}(\theta_x, \theta_y, \theta_z) = \boldsymbol{R}_x(\theta_x)\boldsymbol{R}_y(\theta_y)\boldsymbol{R}_z(\theta_z)\,.$$

We compute the winding tool's orientation by determining the rotation angles $(\theta_x, \theta_y, \theta_z)$ that ensure the local coordinate system rotates synchronously with the Darboux frame as it moves along the base curve $\boldsymbol{\gamma}$ on the surface $\boldsymbol{\sigma}$:

$$\boldsymbol{R}(\theta_x, \theta_y, \theta_z)\boldsymbol{R}_x(\pi/2) = \begin{bmatrix} \boldsymbol{t} & \boldsymbol{B} & \boldsymbol{N} \end{bmatrix}. \tag{36}$$

The constant rotation $\boldsymbol{R}_x(\pi/2)$ accounts for the initial offset between the two frames, ensuring that all rotation angles are zero at $t = -\pi/2$, where the winding tool's coordinate system is aligned with the global frame. By inserting the expressions for $\boldsymbol{t}$, $\boldsymbol{N}$, and $\boldsymbol{B}$ from (1), (33) and (34) into (36) and solving for the rotation angles, we obtain:

$$\theta_x = \arctan(h_y)\,, \tag{37}$$

$$\theta_y = \arcsin\left(-\frac{h_x}{\sqrt{1 + h_x^2 + h_y^2}}\right), \tag{38}$$

$$\theta_z = \arctan 2\left(\frac{\dot{y}\left(1 + h_y^2\right) + \dot{x}h_x h_y}{\sqrt{1 + h_x^2 + h_y^2}}, \dot{x}\right). \tag{39}$$

Figure 13 shows the non-planar superellipse base curve $\boldsymbol{\gamma}$ with the scaled tangent vectors and the resulting winding trajectory $\boldsymbol{\beta}$. The small local coordinate systems along $\boldsymbol{\beta}$ illustrate the rotation of the winding tool.

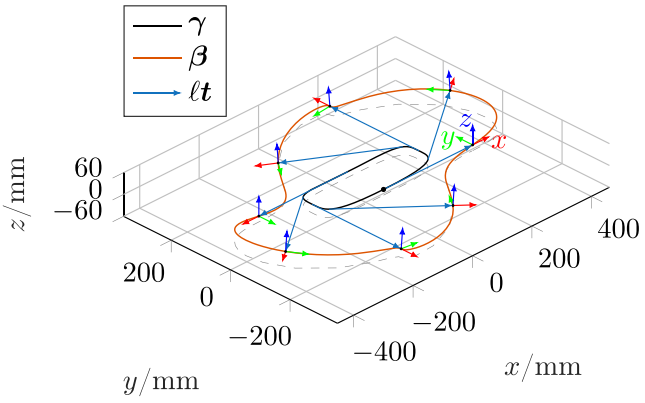

Figure 13. The non-planar superellipse base curve $\boldsymbol{\gamma}$ with scaled tangent vectors and the resulting winding trajectory curve $\boldsymbol{\beta}$. The small local coordinate systems along $\boldsymbol{\beta}$ illustrate the rotation of the winding tool.

5.3.3. Rotating the workpiece positioner. To limit the movement of the winding tool, we want to rotate the workpiece positioner in such a way that the projection of $\boldsymbol{\beta}(t)$ onto the global xy-plane lies on the global x-axis. To determine the rotation angle ψ, let

$$\boldsymbol{\beta}(t) = (\beta_x(t), \beta_y(t), \beta_z(t))\,.$$

The projection of $\boldsymbol{\beta}$ onto the xy-plane is simply $(\beta_x, \beta_y, 0)$. The angle ψ between the global x-axis and a line segment going from the origin to the point $(\beta_x, \beta_y, 0)$ is given by

$$\psi(t) = \arctan 2(\beta_y(t), \beta_x(t))\,. \tag{40}$$

To wind the coil at the point $\boldsymbol{\gamma}(t)$ without rotating the winding tool around the workpiece, the workpiece positioner must instead rotate by the angle $\psi(t)$. For programming the winding tool trajectory, we use a coordinate system that rotates with the positioner. As a result, the winding tool movement is constrained to the xz-plane in the global frame, as it follows the tool trajectory $\boldsymbol{\beta}$ in the rotating coordinate system.

Figure 14 shows the winding tool rotation angles θ_y and θ_z computed from (38) and (39) together with the rotation angle of the workpiece positioner ψ computed with (40) for h given by (25) and the shape parameters listed in table 1. Since this h is independent of y for the non-planar superellipse, we have according to (37), $\theta_x = 0$.

6. Coil design integration

This section estimates the magnetic field and integrates the coil shape into a structural design. We also describe the procedure for constructing the coil assembly. The symbols related to electromagnetism are summarized in table A3.

6.1. Electromagnetic performance

Table 4 lists the specifications of the HTS tape used to wind the coil.

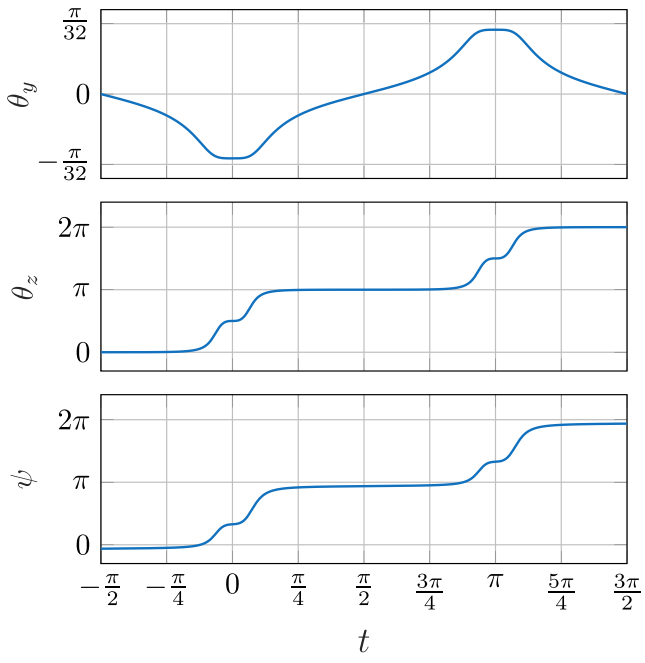

Figure 14. The winding tool rotation angles θ_y and θ_z together with the turntable rotation angle ψ as a function of t. Since h is independent of y, the rotation about the x-axis is $\theta_x = 0$.

Table 4. Specifications for SuperPower SCS4050-AP (2012).

Symbol	Description	Value	Unit
w	Width	4.0	mm
d	Hastelloy thickness	50	µm
d_{cu}	Copper thickness	2×50	µm
d_{cd}	Total tape thickness	155	µm
$I_{\mathrm{c}}(\mathrm{s.f.}, 77K)$	I_{c} at self-field, 77 K	133	A

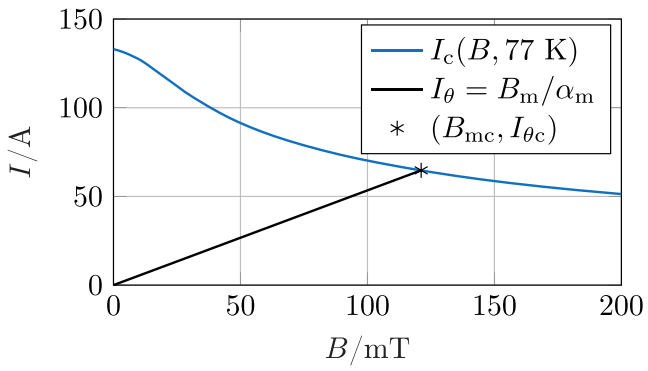

Figure 15. Estimated critical current I_{c} at 77 K for a 4 mm wide SuperPower SCS4050-AP HTS tape, along with the load line of the coil. The intersection gives the coil critical current $I_{\theta\mathrm{c}}$.

Table 5 lists the specified and computed magnet parameters for the non-planar superellipse coil. To maintain focus on the robotic winding process, the number of turns in this demonstration coil is deliberately kept low. As a result, the difference between the peak and central magnetic fields is relatively large.

Table 5. Design parameters for the non-planar superellipse coil.

Symbol	Description	Value	Unit
N	Number of turns	16	—
F_{w}	Winding tension	24	N
v_{w}	Winding speed	1.5	rpm
ℓ	Tangential distance to tool	0.3	m
d_{r}	Coil block radial thickness	2.5	mm
ℓ_{cd}	Conductor length	14	m
T_{op}	Operating temperature	77	K
α_{m}	Peak magnet constant	1.87	$\mathrm{mT\,A^{-1}}$
α_0	Central magnet constant	0.112	$\mathrm{mT\,A^{-1}}$
$I_{\theta\mathrm{c}}$	Coil critical current	64.7	A
B_{mc}	Peak B-field on coil at $I_{\theta\mathrm{c}}$	121	mT
$B_{0\mathrm{c}}$	B-field in center at $I_{\theta\mathrm{c}}$	7.22	mT
L	Self inductance	188	µH
E_{m}	Magnetic energy at $I_{\theta\mathrm{c}}$	393	mJ

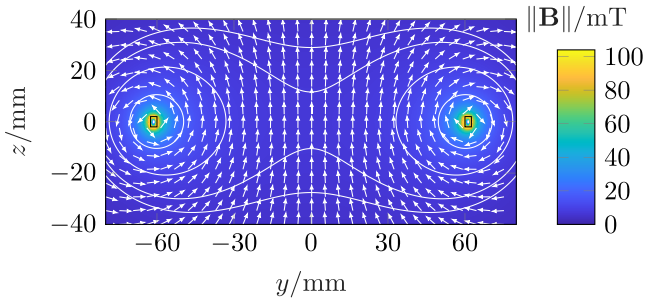

Figure 16. Magnetic flux density in the cross-sectional yz-plane. The color plot represents field magnitude, arrows indicate field direction, and the black lines show the coil boundaries. Closed white curves correspond to contours of constant magnetic field magnitude.

Figure 15 shows the tape's estimated critical current at 77 K together with the load line of the coil. As only self-field measurements of I_{c} are available, the field dependence of the tape's critical current is estimated using data from the HTS wire critical current database [32]. The load line represents the linear relationship between the current in the superconductor I_θ and the peak magnetic field B_{m}, expressed as $B_{\mathrm{m}} = \alpha_{\mathrm{m}} I_\theta$. The peak magnet constant α_{m}, which depends on the coil shape and number of turns, is computed numerically as the ratio of the peak magnetic field to the current. The intersection of the load line with the I_{c}-curve determines the estimated critical current of the coil, $I_{\theta\mathrm{c}}(T_{\mathrm{op}}) = I_{\mathrm{c}}(B_{\mathrm{mc}}, T_{\mathrm{op}})$, where $B_{\mathrm{mc}} = \alpha_{\mathrm{m}} I_{\theta\mathrm{c}}$. Figure 16 shows the magnetic field distribution in the yz-plane, with a strong concentration of flux near the coil.

6.2. *Coil assembly design*

The coil assembly shown in figure 17 consists of a coil former, an inner copper terminal, the winding block, and the outer terminal. The coil former is 3D-printed to realize its complex outer shape. Because the former is too large to be printed in a single piece, it consists of two parts joined by a connector plate. The printing material for the coil former and the connector plate is carbon fiber-reinforced nylon filament

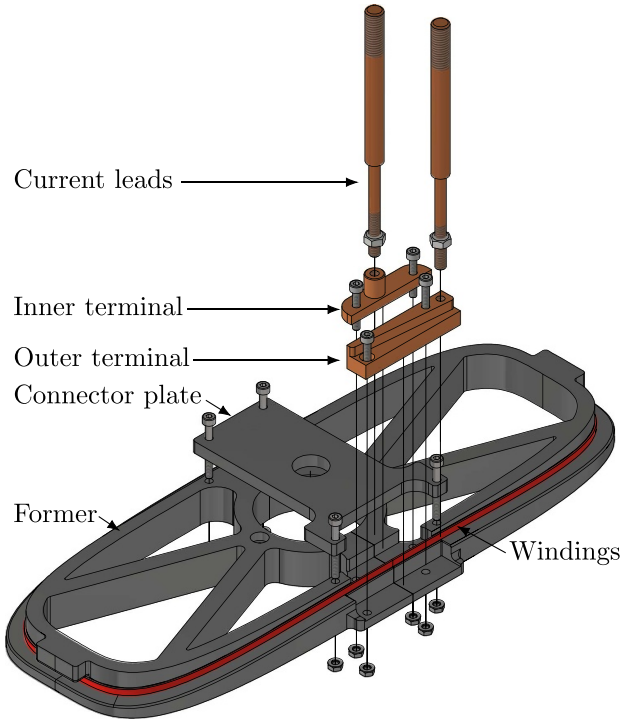

Figure 17. Exploded view of the non-planar superellipse coil assembly. The 3D-printed former is made of carbon fiber reinforced nylon, the inner terminal, outer terminal and current leads are made of copper, while the cap screws and nuts are made of stainless steel.

(Polymaker Fiberon PA6-CF20). While a CNC-machined stainless steel former would have offered better thermal conductivity, the chosen 3D printing material allows rapid prototyping and is relatively easy to process, requiring lower temperatures than many high-performance polymers. Its thermal contraction is comparable to stainless steel, making it suitable for cryogenic applications. The terminals and current leads are machined from copper and fastened to the former using stainless steel cap screws.

6.3. Coil construction

The coil former is fastened to the turntable of the workpiece positioner, and the spool of HTS tape is loaded onto the robotic winding tool. The tape is spooled with the HTS layer facing outward, resulting in an inward-facing orientation on the coil during winding. The contact surfaces of the terminals are pretinned to prepare them for soldering, and the inner terminal is fastened to the coil former. The HTS tape is soldered to the inner terminal to form the initial electrical connection, and the controlled tension is activated. The coil is then wound without insulation using the robotic winding procedure at a speed of 1.5 rpm. A winding tension of 24 N ensures that the tape maintains its hard-way bending and aligns with the shape of the former. Finally, the outer terminal is fastened to the former, and the last turn is soldered to its exterior. Figure 18 shows the completed non-planar coil.

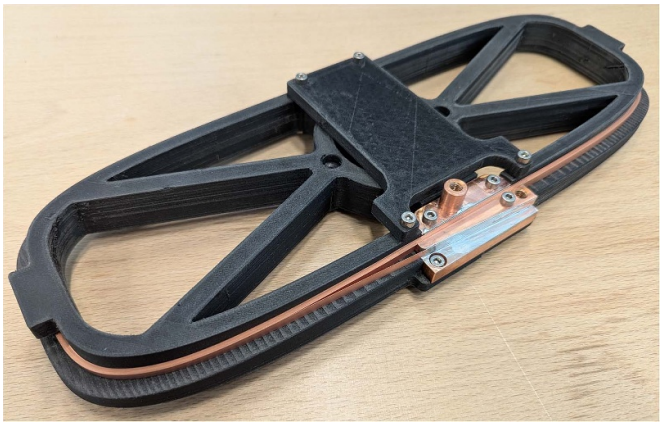

Figure 18. The completed non-planar superellipse coil.

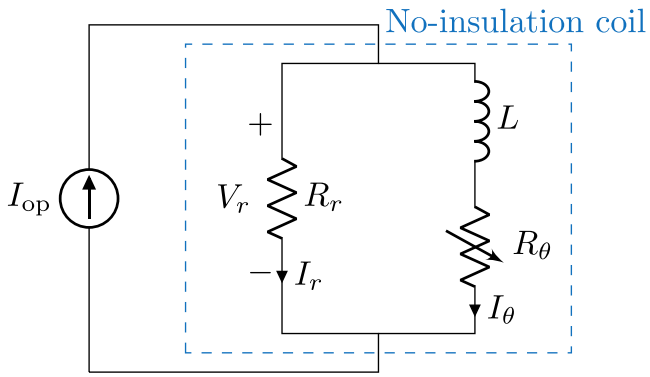

Figure 19. Equivalent circuit diagram for the lumped-element model of a no-insulation coil.

7. Cryogenic measurements

This section outlines the cryogenic characterization of the non-planar no-insulation coil. We present a lumped-element model, describe the measurement procedure, and identify the coil parameters by fitting the model to the data.

7.1. Fitting model

A lumped-element circuit model represents the no-insulation coil [33]. We identify its parameters from the experimental data. Figure 19 depicts the equivalent circuit diagram. A power source controls the operating current $I_{\mathrm{op}}(t)$. At the coil terminal, the current splits into a radial component $I_r(t)$ and an azimuthal component $I_\theta(t)$. By Kirchhoff's Current Law, these are related by

$$I_r = I_{\mathrm{op}} - I_\theta. \tag{41}$$

Along the radial branch, there is the radial resistance R_r representing the sum of the turn-to-turn contact resistances. Along the azimuthal branch, there is the inductance L representing the storage of magnetic energy and an azimuthal resistance R_θ, representing the resistance along the HTS tape modeled by the

phenomenological relationship:

$$R_\theta = R_\mathrm{c}\left(\frac{I_\theta}{I_{\theta\mathrm{c}}}\right)^{n-1}, \quad R_\mathrm{c} = \frac{E_\mathrm{c}\ell_\mathrm{cd}}{I_{\theta\mathrm{c}}} \tag{42}$$

where $I_{\theta\mathrm{c}}$ is the coil critical current at the critical electric field $E_\mathrm{c} = 1\times10^{-4}\,\mathrm{Vm}^{-1}$ and ℓ_cd and ℓ_cd is the length of the conductor. Applying Kirchhoff's voltage law across the two parallel branches, gives the terminal voltage as

$$V_r = R_r I_r = L\dot{I}_\theta + R_\theta I_\theta. \tag{43}$$

The magnetic flux density B_0 at the center of the coil is proportional to the azimuthal current:

$$B_0 = \alpha_0 I_\theta, \tag{44}$$

where α_0 is the central magnet constant. By combining (41), (43) and (44), we obtain

$$V_r = R_r\left(I_\mathrm{op} - \frac{1}{\alpha_0}B_0\right) \tag{45}$$

which relates the terminal voltage to the measured magnetic field and operating current. This expression enables the identification of the radial resistance R_r from measurements of I_op, V_r, and B_0. Differentiating (44) with respect to time and substituting $\dot{I}_\theta$ from (43) yields

$$\dot{B}_0 = \frac{R_r + R_\theta}{L}\left(\alpha_0\frac{R_r}{R_r+R_\theta}I_\mathrm{op} - B_0\right). \tag{46}$$

This expression is used to determine the time constant $\tau_\mathrm{c} = L/R_r$, as well as the power-law parameters n and $I_{\theta\mathrm{c}}$. We assume a constant temperature during operation, and a fixed critical current $I_{\theta\mathrm{c}}$. As a result, the model does not capture thermal effects or quench dynamics, and its accuracy may decrease when the operating current approaches or exceeds $I_{\theta\mathrm{c}}$, where local heating arising from current redistribution becomes significant.

7.2. Experimental setup

Voltage taps are placed on the coil terminals to measure the voltage drop V_r across the coil. A Hall probe positioned at the origin of the coil coordinate system measures the magnetic flux density. Nanovoltmeters connected to a computer record the voltage signals from the V_r voltage taps and the Hall probe, while the operating current I_op is measured using a multimeter. The coil is mounted on a support plate with extended handles, allowing safe immersion into and retrieval from the cryogenic bath. The support plate is inserted into a thermally insulated container, which is then slowly filled with liquid nitrogen until the entire coil and the lower part of the current leads are fully submerged. A 4-quadrant linear power amplifier supplies a current of up to 250 A to the coil. The current is controlled using an external ramp generator.

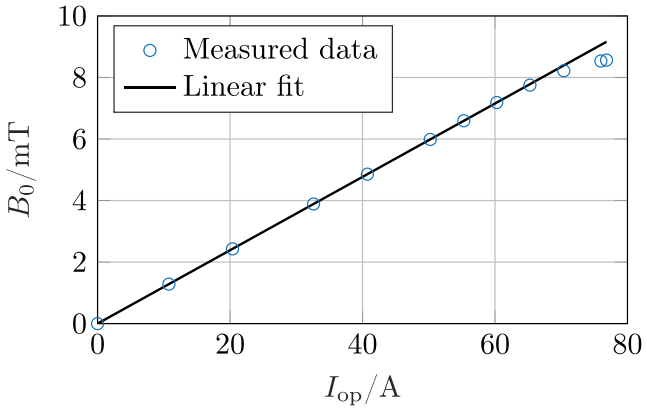

Figure 20. Measured data steady-state pairs of central magnetic flux density B_0 and operating current I_op, along with the fitted line of slope α_0.

7.3. Measurement procedure

We divide the measurements into three series, each targeting specific model parameters. In the first series, we aim to determine the magnet constant α_0. The operating current I_op is increased to a specified target value and held constant for approximately 120 s to ensure steady-state conditions. This procedure is repeated for multiple target currents. The second series follows the same procedure but uses faster current ramp rates to generate transient data for identifying the radial resistance R_r and time constant τ_c. In the third series, we slowly ramp the current beyond the critical current to collect data for determining the coil's critical current $I_{\theta\mathrm{c}}$ and the power law exponent n.

7.4. Parameter identification

When the operating current I_op is held constant and remains well below the critical current of the coil, the azimuthal resistance becomes negligible, $R_\theta \approx 0$, and the azimuthal current converges to the operating current. The steady-state magnetic field B_0 in the coil center then satisfies

$$\lim_{t\to\infty} B_0(t) = \alpha_0 I_\mathrm{op}. \tag{47}$$

By inserting measured steady-state values of I_op and B_0 into (47), we determine the magnet constant α_0 through linear regression in the low-current regime. Figure 20 shows the measured steady-state pairs together with the fitted line of slope α_0.

Once α_0 is determined, the radial resistance R_r is obtained by substituting measured values of V_r and B_0 into (45) and solving the resulting linear regression problem. The specific contact resistivity ρ_r is then given by $\rho_r = AR_r$, where $A = w\ell_\mathrm{cd}$ is the contact surface area.

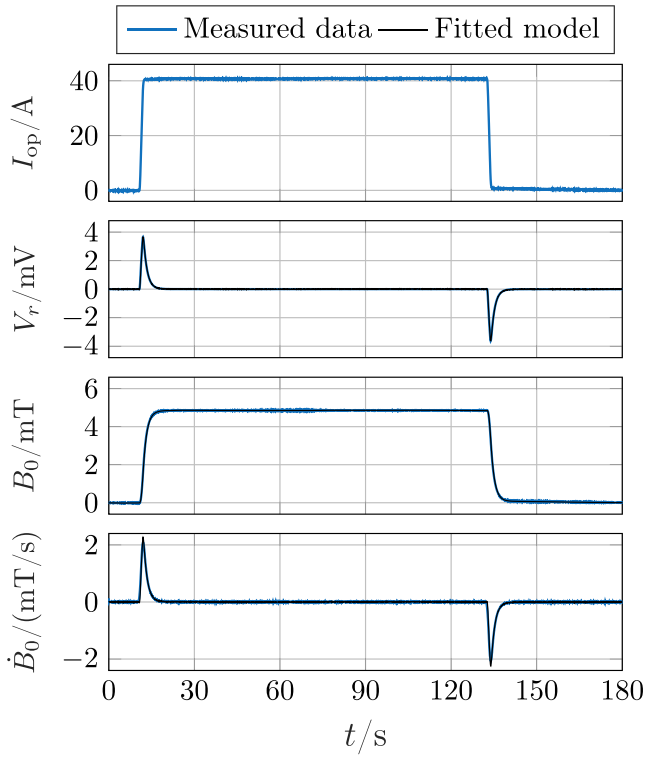

Figure 21. Measured and model values of the operating current, I_{op}, voltage drop across the coil V_r, magnetic flux density B_0, and its time-derivative $\dot{B}_0$ as functions of time. The current is ramped up at a rate of approximately 40 A s^{-1}, held constant, and then ramped down. The measured data for I_{op}, V_r and B_0 was used to determine R_r, while the data for I_{op}, B_0 and $\dot{B}_0$ was used to determine τ_c.

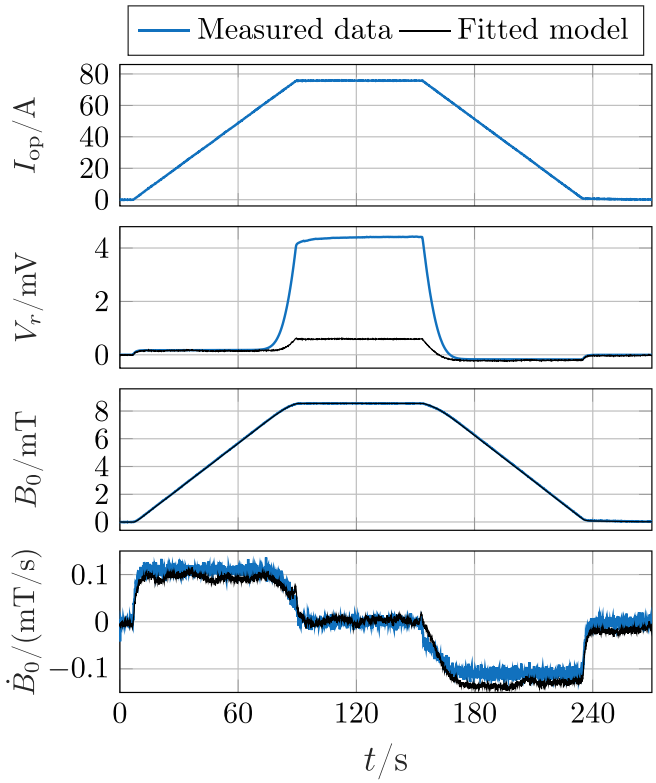

Figure 22. Measured and fitted data of the operating current, I_{op}, voltage drop across the coil V_r, magnetic flux density B_0, and its time-derivative $\dot{B}_0$ as functions of time. The current is ramped up at a rate of approximately 1 A s^{-1}, held constant, and then ramped down. The measured data for I_{op}, B_0 and $\dot{B}_0$ were used to determine n and $I_{\theta c}$.

When the operating current is well below the critical current, such that $R_\theta \approx 0$, (46) reduces to

$$\lim_{R_\theta \to 0} \dot{B}_0 = \frac{1}{\tau_c}(\alpha_0 I_{op} - B_0) \tag{48}$$

where $\tau_c = L/R_r$ is the charging time constant. The time constant τ_c is estimated by inserting measured values of I_{op}, $\dot{B}_0$ and B_0 into (48) and solving the resulting linear regression problem. The self-inductance is subsequently calculated by $L = \tau_c R_r$. Figure 21 displays the data set used to determine R_r and τ_c, along with the corresponding model fit.

To complete the parameter identification, we perform a nonlinear fit of (46) to determine the power law exponent n and the coil critical current $I_{\theta c}$, treating both as fitting parameters. The fit is based on a measured data set in which I_{op} is ramped above the critical current and then decreased again. The fitting is performed without using V_r data. Figure 22 displays the data set used to determine $I_{\theta c}$ and n, along with the corresponding model fit. The magnetic energy is calculated as $E_m = \frac{1}{2} L I_{\theta c}^2$, using the inductance and critical current values fitted from measurements. Table 6 summarizes the parameters identified from the measurement data. The critical current shows no sign of degradation.

Table 6. Measured magnet parameters for the non-planar superellipse coil. The standard errors of the fitted parameters are smaller than the precision shown, except for the power-law exponent n, which has a standard error of 0.3.

Symbol	Description	Value	Unit
α_0	Central magnet constant	0.119	mT A^{-1}
R_r	Radial resistance	151	μΩ
A	Contact surface area	560	cm^2
ρ_r	Specific contact resistivity	84.6	mΩ cm^2
τ_c	Charging time constant	1.27	s
L	Self inductance	192	μH
n	Power law exponent	29.5	—
$I_{\theta c}$	Coil critical current	74.0	A
E_m	Magnetic energy at $I_{\theta c}$	526	mJ

While the model fits the data for B_0 and $\dot{B}_0$ well, it underestimates V_r near the critical current, likely due to its lack of temperature dependence. Figure 23 shows the measured steady-state pairs of V_r and I_{op}, together with the corresponding model predictions from (45). The modeled values are computed using the steady-state B_0 data from figure 20 and the previously determined parameters R_r and α_0. The model reproduces V_r accurately at currents well below $I_{\theta c}$ but deviates near and above it.

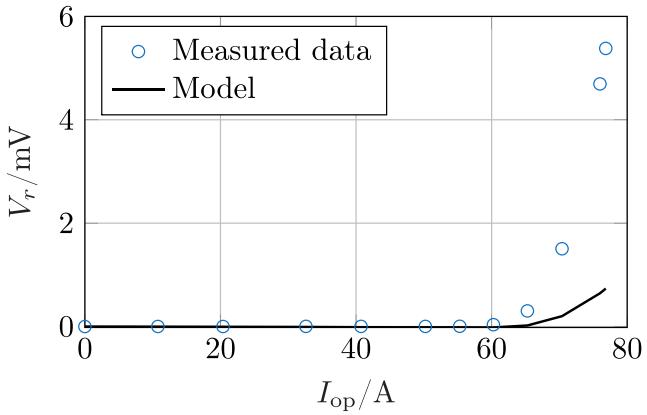

Figure 23. Measured steady-state pairs of terminal voltage V_r and operating current I_{op}, together with the model prediction from (45) using the previously determined values of R_r and α_0.

8. Conclusion

We demonstrate a robotic winding approach for non-planar HTS coils through the design, construction, and cryogenic testing of an superellipse-shaped HTS coil with hard-way bending. We apply a differential geometry approach to design the coil shape while adhering to strain constraints in the HTS layer. From the coil shape, we derive the winding tool trajectory and rotations. The coil is wound using a robotic system, and electromagnetic characterization at 77 K verifies its performance. We determine characteristic coil parameters by fitting a lumped-element circuit model to the measurement data. The results confirm that non-planar no-insulation HTS coils, designed using the differential geometry approach, can be reliably constructed using this robotic winding setup without degradation of the critical current.

Future work will aim to extend the current method to accommodate a broader range of coil geometries. Very complex shapes, such as concave sections or winding paths looping through openings, would require the development of new robotic winding techniques. While the winding method described here only requires the positioner and a single articulated robot, these advanced techniques may involve the second articulated robot in our setup, using a dedicated tool to support the process.

Data availability statement

The data cannot be made publicly available upon publication because no suitable repository exists for hosting data in this field of study. The data that support the findings of this study are available upon reasonable request from the authors.

Acknowledgments

The authors thank the staff at the KIT magnet laboratory for their support in coil construction and cryogenic testing.

Table A1. Symbols related to geometry.

Symbol	Description	Unit
A	Contact surface area	m^2
a	Semi-major axis	m
$\boldsymbol{\alpha}$	Surface representing HTS layer	—
$\boldsymbol{B}$	Intrinsic normal to surface	—
b	Semi-minor axis	m
$\boldsymbol{b}$	Unit binormal vector	—
$\boldsymbol{\beta}$	Winding tool trajectory	—
β_x,β_y,β_z	Components of $\boldsymbol{\beta}$	—
d	Substrate thickness	m
d_r	Coil block radial width	m
d_{cd}	Tape thickness	m
d_{cu}	Copper thickness	m
$\boldsymbol{\delta}$	Ruling direction	—
$\boldsymbol{\eta}$	Non-planar surface	—
$\boldsymbol{\Gamma}$	Striction curve of ruled surface	—
$\boldsymbol{\gamma}$	Base curve of ruled surface	—
h	Function defining the non-planarity	—
K	Gaussian curvature	m^{-1}
κ	Curvature	m^{-1}
κ_{g}	Geodesic curvature	m^{-1}
κ_{g0}	Central geodesic curvature	m^{-1}
κ_{n}	Normal curvature	m^{-1}
ℓ	Tangential distance to tool	m
ℓ_{cd}	Conductor length	m
m	Shape exponent	—
$\boldsymbol{N}$	Normal vector to surface	—
$\boldsymbol{n}$	Unit normal vector	—
$\boldsymbol{\omega}$	Darboux vector	—
ψ	Rotation angle for positioner	rad
$\boldsymbol{R}_i$	Rotation matrix around i-axis	—
r	Radial coordinate	—
$\mathbb{R}^k$	k-dimensional real space	—
s	Arc-length of curve	—
$\mathrm{SO}(3)$	Special orthogonal group in 3D	—
$\boldsymbol{\sigma}$	Ruled surface	—
t	Parameter along base curve	—
$\boldsymbol{t}$	Unit tangent vector	—
τ	Torsion	m^{-1}
τ_{g}	Geodesic torsion	m^{-1}
τ_{t}	Twist rate	m^{-1}
θ	Angle between $\boldsymbol{N}$ and $\boldsymbol{n}$	rad
θ_x, θ_y, θ_z	Rotation angles for winding tool	rad
U	Subset of $\mathbb{R}^2$	—
v	Parameter along rulings	m
w	Tape width	m
x,y,z	Cartesian coordinates	—

Appendix A. List of symbols

The list of symbols is divided into three categories: table A1 for geometry, table A2 for mechanics, and table A3 for electromagnetism.

Appendix B. Strain derivation

We derive the expressions for the normal, geodesic, and twisting strain given in (16)–(18).

Table A2. Symbols related to mechanics.

Symbol	Description	Unit
ε	Engineering strain	—
ε_{n}	Normal strain	—
ε_{g}	Geodesic strain	—
ε_{t}	Twisting strain	—
ε_{i}	Total intrinsic strain	—
$\varepsilon_{\mathrm{n,min}}$	Minimum normal strain	—
$\varepsilon_{\mathrm{n,max}}$	Maximum normal strain	—
$\varepsilon_{\mathrm{g,min}}$	Minimum geodesic strain	—
$\varepsilon_{\mathrm{g,max}}$	Maximum geodesic strain	—
$\varepsilon_{\mathrm{t,min}}$	Minimum twisting strain	—
$\varepsilon_{\mathrm{t,max}}$	Maximum twisting strain	—
$\varepsilon_{\mathrm{i,min}}$	Minimum total intrinsic strain	—
$\varepsilon_{\mathrm{i,max}}$	Maximum total intrinsic strain	—
$\varepsilon_{\mathrm{min}}$	Irreversible compressive strain limit	—
$\varepsilon_{\mathrm{max}}$	Irreversible tensile strain limit	—
λ	Mid-surface to HTS layer distance	m
F_{w}	Winding tension	N
v_{w}	Winding speed	rpm
l	Length after deformation	m
l_0	Length before deformation	m

Table A3. Symbols related to electromagnetism.

Symbol	Description	Unit
α_0	Central magnet constant	$\mathrm{T\,A^{-1}}$
α_{m}	Peak magnet constant	$\mathrm{T\,A^{-1}}$
B_0	Central magnetic field	T
$B_{0\mathrm{c}}$	B-field in center at $I_{\theta\mathrm{c}}$	T
B_{m}	Peak B-field on coil	T
B_{mc}	Peak B-field on coil at $I_{\theta\mathrm{c}}$	T
E_{c}	Critical electric field	$\mathrm{V\,m^{-1}}$
E_{m}	Magnetic energy at $I_{\theta\mathrm{c}}$	J
I_{c}	Tape critical current	A
I_{op}	Operating current	A
I_r	Radial current	A
I_θ	Azimuthal current	A
$I_{\theta\mathrm{c}}$	Coil critical current	A
L	Self inductance	H
N	Number of turns	—
n	Power law exponent	—
R_{c}	Critical azimuthal resistance	Ω
R_r	Radial resistance	Ω
R_θ	Azimuthal resistance	Ω
ρ_r	Specific contact resistivity	$\Omega\,\mathrm{m^2}$
t	Time	s
T_{op}	Operating temperature	K
τ_{c}	Charging time constant	s
V_r	Voltage across coil	V

B.1. Normal strain

We consider a helical base curve $\boldsymbol{\gamma}_{\mathrm{n}}(t) = (x(t), y(t), z(t))^{\intercal}$ with constant positive curvature $\kappa = \kappa_0 > 0$ and torsion $\tau = \tau_0$:

$$x(t) = \frac{\kappa_0}{\kappa_0^2 + \tau_0^2}\cos t,$$
$$y(t) = \frac{\kappa_0}{\kappa_0^2 + \tau_0^2}\sin t,$$
$$z(t) = \frac{\tau_0 t}{\kappa_0^2 + \tau_0^2}.$$

The tangent vector $\dot{\boldsymbol{\gamma}}_{\mathrm{n}}(t) = (\dot{x}(t), \dot{y}(t), \dot{z}(t))^{\intercal}$ is

$$\dot{\boldsymbol{\gamma}}_{\mathrm{n}}(t) = \frac{1}{\kappa_0^2 + \tau_0^2}\begin{pmatrix} -\kappa_0 \sin t \\ \kappa_0 \cos t \\ \tau_0 \end{pmatrix}.$$

The speed $\|\dot{\boldsymbol{\gamma}}_{\mathrm{n}}\| = 1/\sqrt{\kappa_0^2 + \tau_0^2}$ confirms that $\boldsymbol{\gamma}_{\mathrm{n}}$ is regular. The unit tangent vector $\boldsymbol{t}$ is then

$$\boldsymbol{t}(t) = \frac{1}{\sqrt{\kappa_0^2 + \tau_0^2}}\begin{pmatrix} -\kappa_0 \sin t \\ \kappa_0 \cos t \\ \tau_0 \end{pmatrix}$$

and the unit normal vector is

$$\boldsymbol{n}(t) = \frac{\dot{\boldsymbol{t}}}{\|\dot{\boldsymbol{t}}\|} = \begin{pmatrix} -\cos t \\ -\sin t \\ 0 \end{pmatrix}.$$

The binormal vector is

$$\boldsymbol{b}(t) = \boldsymbol{t} \times \boldsymbol{n} = \frac{1}{\sqrt{\kappa_0^2 + \tau_0^2}}\begin{pmatrix} \tau_0 \sin t \\ -\tau_0 \cos t \\ \kappa_0 \end{pmatrix}.$$

The Darboux vector is obtained as

$$\boldsymbol{\omega} = \tau \boldsymbol{t} + \kappa \boldsymbol{b} = \begin{pmatrix} 0 \\ 0 \\ \sqrt{\kappa_0^2 + \tau_0^2} \end{pmatrix}.$$

We choose the ruling direction parallel to the unit Darboux vector, $\boldsymbol{\delta} = \boldsymbol{\omega}/\|\boldsymbol{\omega}\| = (0,0,1)^{\intercal}$. The resulting ruled surface,

$$\boldsymbol{\sigma}_{\mathrm{n}}(t, v) = \boldsymbol{\gamma}_{\mathrm{n}}(t) + v\boldsymbol{\delta}(t),$$

is the rectifying developable of $\boldsymbol{\gamma}_{\mathrm{n}}$. The surface normal along $\boldsymbol{\gamma}_{\mathrm{n}}$ is $\boldsymbol{N} = -\boldsymbol{n}$, and the intrinsic normal is $\boldsymbol{B} = \boldsymbol{b}$. The normal curvature is

$$\kappa_{\mathrm{n}} = \frac{\ddot{\boldsymbol{\gamma}}_{\mathrm{n}} \cdot \boldsymbol{N}}{\|\dot{\boldsymbol{\gamma}}_{\mathrm{n}}\|^2} = -\kappa_0.$$

Reversing the parameterization of either $\boldsymbol{\gamma}_{\mathrm{n}}$ or $\boldsymbol{\delta}$ changes the sign of κ_{n}. Because both parameterizations represent the same surface, the surface geometry is equivalently characterized by $\kappa_{\mathrm{n}} = \pm\kappa_0$. The geodesic curvature is

$$\kappa_{\mathrm{g}} = \frac{\ddot{\boldsymbol{\gamma}}_{\mathrm{n}} \cdot \boldsymbol{B}}{\|\dot{\boldsymbol{\gamma}}_{\mathrm{n}}\|^2} = 0.$$

The derivative of the surface normal is $\dot{\boldsymbol{N}} = (-\sin t, \cos t, 0)^{\intercal}$, giving $\boldsymbol{N} \times \dot{\boldsymbol{N}} = (0,0,1)^{\intercal}$. Hence, the geodesic torsion is

$$\tau_{\mathrm{g}} = \frac{\dot{\boldsymbol{\gamma}}_{\mathrm{n}} \cdot (\boldsymbol{N} \times \dot{\boldsymbol{N}})}{\|\dot{\boldsymbol{\gamma}}_{\mathrm{n}}\|^2} = \frac{\dot{z}}{\|\dot{\boldsymbol{\gamma}}_{\mathrm{n}}\|^2} = \tau_0.$$

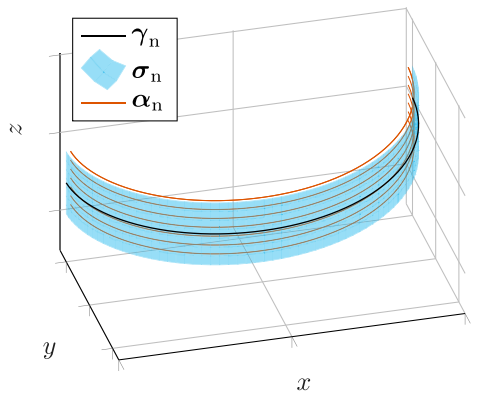

Figure B1. The helical base curve γ_n, the ruled surface σ_n and the family of curves representing the HTS layer α_n used to derive the normal strain ε_n.

Since $\tau = \tau_0$, the twist rate is $\tau_t = \tau_g - \tau = 0$. The HTS layer is represented by a family of curves offset by a distance λ from the ruled surface along the surface normal:

$$\boldsymbol{\alpha}_n(t;v) = \boldsymbol{\sigma}_n(t,v) - \lambda \boldsymbol{N}(t),$$

where $v \in [-w/2, w/2]$ and $t \in [0, t_0]$. Figure B1 shows the relations between γ_n, σ_n, and α_n.

The tangent vector to α_n is

$$\dot{\boldsymbol{\alpha}}_n(t;v) = \frac{1}{\kappa_0^2+\tau_0^2}\begin{pmatrix} \left(\kappa_0 + \lambda\left(\kappa_0^2+\tau_0^2\right)\right)\sin t \\ -\left(\kappa_0 + \lambda\left(\kappa_0^2+\tau_0^2\right)\right)\cos t \\ \tau_0 \end{pmatrix}$$

and its norm is

$$\|\dot{\boldsymbol{\alpha}}_n\| = \frac{\sqrt{(1+\lambda\kappa_0)^2 + (\lambda\tau_0)^2}}{\sqrt{\kappa_0^2+\tau_0^2}}.$$

The deformed length of α_n is

$$l = \int_0^{t_0} \|\dot{\boldsymbol{\alpha}}_n\| \, \mathrm{d}t = \frac{t_0\sqrt{(1+\lambda\kappa_0)^2 + (\lambda\tau_0)^2}}{\sqrt{\kappa_0^2+\tau_0^2}}.$$

The undeformed length of α_n equals the deformed length of γ_n,

$$l_0 = \int_0^{t_0} \|\dot{\gamma}_n\| \mathrm{d}t = \frac{t_0}{\sqrt{\kappa_0^2+\tau_0^2}}.$$

The engineering strain is therefore

$$\varepsilon_n = \frac{l-l_0}{l_0} = \sqrt{(1+\lambda\kappa_0)^2 + (\lambda\tau_0)^2} - 1. \tag{B.1}$$

Substituting $\kappa_0 = \pm\kappa_n$ and $\tau_0 = \tau$ into (B.1) yields (16).

B.2. Geodesic strain

We consider a circular-arc base curve $\gamma_g(t) = (x(t), y(t), z(t))^\intercal$ with constant positive curvature $\kappa = \kappa_0 > 0$ and zero torsion $\tau = 0$:

$$x(t) = \frac{1}{\kappa_0}\cos t,$$
$$y(t) = 0,$$
$$z(t) = \frac{1}{\kappa_0}\sin t.$$

The tangent vector $\dot{\gamma}_g(t) = (\dot{x}(t), \dot{y}(t), \dot{z}(t))^\intercal$ is

$$\dot{\boldsymbol{\gamma}}_g(t) = \frac{1}{\kappa_0}\begin{pmatrix} -\sin t \\ 0 \\ \cos t \end{pmatrix}.$$

The speed $\|\dot{\gamma}_g\| = 1/\kappa_0$ confirms that γ_n is regular. The unit tangent vector $\boldsymbol{t}$ is then

$$\boldsymbol{t}(t) = \begin{pmatrix} -\sin t \\ 0 \\ \cos t \end{pmatrix}$$

and the unit normal vector is

$$\boldsymbol{n}(t) = \frac{\dot{\boldsymbol{t}}}{\|\dot{\boldsymbol{t}}\|} = \begin{pmatrix} -\cos t \\ 0 \\ -\sin t \end{pmatrix}.$$

The binormal vector is

$$\boldsymbol{b}(t) = \boldsymbol{t} \times \boldsymbol{n} = \begin{pmatrix} 0 \\ -1 \\ 0 \end{pmatrix}.$$

We choose the ruling direction parallel to the normal vector $\boldsymbol{\delta} = \boldsymbol{n}$. The resulting ruled surface,

$$\boldsymbol{\sigma}_g(t,v) = \boldsymbol{\gamma}_g(t) + v\boldsymbol{n}(t),$$

is the normal developable of γ_g. The surface normal along γ_g is $\boldsymbol{N} = \boldsymbol{b}$, and the intrinsic normal is $\boldsymbol{B} = \boldsymbol{n}$. The normal curvature is

$$\kappa_n = \frac{\ddot{\boldsymbol{\gamma}}_g \cdot \boldsymbol{N}}{\|\dot{\boldsymbol{\gamma}}_g\|^2} = 0,$$

and the geodesic curvature is

$$\kappa_g = \frac{\ddot{\boldsymbol{\gamma}}_g \cdot \boldsymbol{B}}{\|\dot{\boldsymbol{\gamma}}_g\|^2} = \kappa_0.$$

Reversing the ruling direction changes the sign of κ_g. Because both parameterizations represent the same surface, the surface geometry is equivalently characterized by $\kappa_g = \pm\kappa_0$. The derivative of the surface normal is $\dot{\boldsymbol{N}} = \boldsymbol{0}$. Hence, the geodesic torsion is

$$\tau_g = \frac{\dot{\boldsymbol{\gamma}}_g \cdot (\boldsymbol{N} \times \dot{\boldsymbol{N}})}{\|\dot{\boldsymbol{\gamma}}_g\|^2} = 0.$$

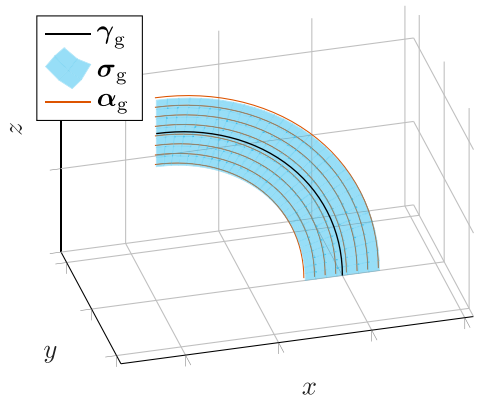

Figure B2. The circular-arc base curve γ_g, the ruled surface σ_g and the family of curves representing the HTS layer α_g used to derive the geodesic strain ε_g.

Since $\tau = 0$, the twist rate is $\tau_t = \tau_g - \tau = 0$. The HTS layer is represented by a family of curves offset by a distance λ from the ruled surface along the surface normal:

$$\boldsymbol{\alpha}_g(t;v) = \boldsymbol{\sigma}_g(t,v) - \lambda \boldsymbol{N}(t),$$

where $v \in [-w/2, w/2]$ and $t \in [0, t_0]$. Figure B2 shows the relations between γ_g, σ_g, and α_g.

The tangent vector to α_g is

$$\dot{\boldsymbol{\alpha}}_g(t;v) = \left(\frac{1}{\kappa_0} - v\right)\begin{pmatrix} -\sin t \\ 0 \\ \cos t \end{pmatrix}$$

and its norm is

$$\|\dot{\boldsymbol{\alpha}}_g\| = \frac{1}{\kappa_0} - v.$$

The deformed length of α_g is

$$l = \int_0^{t_0} \|\dot{\boldsymbol{\alpha}}_g\|\,\mathrm{d}t = \left(\frac{1}{\kappa_0} - v\right) t_0.$$

The undeformed length of α_g equals the deformed length of γ_g,

$$l_0 = \int_0^{t_0} \|\dot{\boldsymbol{\gamma}}_g\|\mathrm{d}t = \frac{t_0}{\kappa_0}.$$

The engineering strain is therefore

$$\varepsilon_g = \frac{l - l_0}{l_0} = -v\kappa_0. \tag{B.2}$$

Substituting $\kappa_0 = \pm\kappa_g$ into (B.2) yields (17).

B.3. Twisting strain

We consider a linear base curve $\gamma_t(t) = (x(t), y(t), z(t))^\intercal$ with zero curvature $\kappa = 0$ and torsion $\tau = 0$:

$$\begin{aligned} x(t) &= t, \\ y(t) &= 0, \\ z(t) &= 0. \end{aligned}$$

The curve is unit-speed, so the tangent vector is $\dot{\boldsymbol{\gamma}}_t(t) = \boldsymbol{t} = \boldsymbol{e}_x$. We choose the ruling direction to be initially along the z-axis, and rotating about the x-axis with a twist rate τ_0,

$$\boldsymbol{\delta}(t) = \boldsymbol{R}_x(\tau_0 t)\,\boldsymbol{e}_z = \begin{pmatrix} 0 \\ -\sin(\tau_0 t) \\ \cos(\tau_0 t) \end{pmatrix}$$

The resulting ruled surface.

$$\boldsymbol{\sigma}_t(t,v) = \boldsymbol{\gamma}_t(t) + v\boldsymbol{\delta}(t),$$

twists about the base curve γ_t. Because the curvature is zero, $\kappa = 0$, both the normal and geodesic curvatures vanish, $\kappa_n = 0$ and $\kappa_g = 0$. The surface normal along γ_t is

$$\boldsymbol{N} = \begin{pmatrix} 0 \\ -\cos(\tau_0 t) \\ -\sin(\tau_0 t) \end{pmatrix},$$

and the derivative of the surface normal is

$$\dot{\boldsymbol{N}} = \begin{pmatrix} 0 \\ \tau_0 \sin(\tau_0 t) \\ -\tau_0 \cos(\tau_0 t) \end{pmatrix}.$$

Hence $\boldsymbol{N} \times \dot{\boldsymbol{N}} = \tau_0 \boldsymbol{e}_x$, and the geodesic torsion is

$$\tau_g = \frac{\dot{\boldsymbol{\gamma}}_t \cdot (\boldsymbol{N} \times \dot{\boldsymbol{N}})}{\|\dot{\boldsymbol{\gamma}}_t\|^2} = \tau_0.$$

Since $\tau = 0$, the twist rate is $\tau_t = \tau_g - \tau = \tau_0$. The HTS layer is represented by a family of curves offset by a distance λ from the ruled surface along the surface normal:

$$\boldsymbol{\alpha}_t(t;v) = \boldsymbol{\sigma}_t(t,v) - \lambda \boldsymbol{N}(t),$$

where $v \in [-w/2, w/2]$ and $t \in [0, t_0]$. Figure B3 shows the relations between γ_t, σ_t, and α_t.

The tangent vector to α_t is

$$\dot{\boldsymbol{\alpha}}_t(t;v) = \begin{pmatrix} 1 \\ -v\tau_0\cos(\tau_0 t) - \lambda\tau_0\sin(\tau_0 t) \\ -v\tau_0\sin(\tau_0 t) + \lambda\tau_0\cos(\tau_0 t) \end{pmatrix}$$

and its norm is

$$\|\dot{\boldsymbol{\alpha}}_t\| = \sqrt{1 + (v^2 + \lambda^2)\tau_0^2}.$$

The deformed length of α_t is

$$l = \int_0^{t_0} \|\dot{\boldsymbol{\alpha}}_t\|\,\mathrm{d}t = t_0\sqrt{1 + (v^2 + \lambda^2)\tau_0^2}.$$

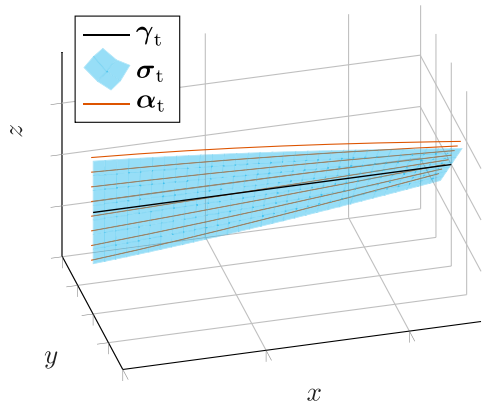

Figure B3. The linear base curve γ_t, the ruled surface σ_t and the family of curves representing the HTS layer α_t used to derive the twisting strain ε_t.

The undeformed length of α_t equals the deformed length of γ_t,

$$l_0 = \int_0^{t_0} \|\dot{\gamma}_t\| \mathrm{d}t = t_0.$$

The engineering strain is therefore

$$\varepsilon_t = \frac{l - l_0}{l_0} = \sqrt{1 + (v^2 + \lambda^2)\,\tau_0^2} - 1. \tag{B.3}$$

Substituting $\tau_0 = \tau_t$ into (B.3) yields (18).

ORCID iDs

Magnus Dam 0000-0002-6707-9548
Tabea Arndt 0000-0002-7797-8862

References

[1] van Nugteren J, Kirby G, de Rijk G, Rossi L, ten Kate H and Dhalle M 2014 *IEEE Trans. Appl. Supercond.* **25** 4000705
[2] Kim G *et al* 2023 *Supercond. Sci. Technol.* **36** 084002
[3] Vargas-Llanos C R, Huber F, Riva N, Zhang M and Grilli F 2022 *Supercond. Sci. Technol.* **35** 124001
[4] van Nugteren J, Kirby G, Murtomäki J, de Rijk G, Rossi L and Stenvall A 2018 *IEEE Trans. Appl. Supercond.* **28** 4008509
[5] De Matteis E *et al* 2024 *IEEE Trans. Appl. Supercond.* **34** 4402505
[6] Du J, Zeng Z, Zhang G, Zhao K, Liu T, Zhao Y, Wu Q and Zhan T 2025 *Physica C* **630** 1354667
[7] Radovinsky A, Kuznetsov S and Brunner D 2024 *IEEE Trans. Appl. Supercond.* **34** 4204904
[8] Shneerson G, Voloshin K, Titkov V, Rodin I Y, Zapretilina E, Hon T, Hitrov N, Ovsyannikov V and Lantsetov A 2024 *IEEE Trans. Appl. Supercond.* **34** 5701204
[9] Richter S, Ballarino A, Bernhard A and Muller A-S 2024 *IEEE Trans. Appl. Supercond.* **34** 4101507
[10] Backmeyer M, Riva N, Lyly M, Halbach A and Lahtinen V 2024 *IEEE Trans. Appl. Supercond.* **34** 4202205
[11] Lion J *et al* 2025 *Fusion Eng. Des.* **214** 114868
[12] Oomen M P, Leghissa M, Proelss N and Neumueller H-W 2009 *IEEE Trans. Appl. Supercond.* **19** 1633–8
[13] Yang S, Song W, Park J, Kim G, Huang J Y, Hahn S, Choi S, Kang H and Hahn G 2024 *IEEE Trans. Appl. Supercond.* **34** 4801304
[14] Wang X, Arbelaez D, Caspi S, Prestemon S O, Sabbi G and Shen T 2017 *IEEE Trans. Appl. Supercond.* **27** 6604010
[15] Takayasu M, Chiesa L, Bromberg L and Minervini J V 2011 *Supercond. Sci. Technol.* **25** 014011
[16] Cook J 1991 *IEEE Trans. Magn.* **27** 1976–80
[17] Russenschuck S 2011 *Field Computation for Accelerator Magnets: Analytical and Numerical Methods for Electromagnetic Design and Optimization* (Elsevier) ch 19, pp 609–36
[18] Auchmann B and Russenschuck S 2004 *IEEE Trans. Magn.* **40** 1208–11
[19] Nes T, Kirby G, De Rijk G, Canale M, Gentini L, Van Nugteren J, Kario A and Ten Kate H 2022 *IEEE Trans. Appl. Supercond.* **32** 4002105
[20] Huslage P, Kulla D, Lobsien J-F, Schuler T and Stenson E V 2024 *Supercond. Sci. Technol.* **37** 085010
[21] Nes T, de Rijk G, Kario A and Ten Kate H 2022 *Supercond. Sci. Technol.* **35** 105011
[22] Liebsch M and Russenschuck S 2023 *IEEE Trans. Appl. Supercond.* **34** 4900205
[23] Pressley A N 2010 *Elementary Differential Geometry* (Springer) ch 2, pp 29–54
[24] Gallier J 2011 *Geometric Methods and Applications: for Computer Science and Engineering* (Springer) ch 20 , pp 585–654
[25] Arslan K, Bulca B and Öztürk G 2021 *Turk. J. Sci.* **6** 36–44
[26] Honda S 2018 *Adv. Stud. Pure Math.* **78** 273–93
[27] Izumiya S, Romero Fuster M d C, Ruas M A S and Tari F 2016 *Differential Geometry From a Singularity Theory Viewpoint* (World Scientific) ch 1, pp 1–22
[28] Paz-Soldan C 2020 *J. Plasma Phys.* **86** 815860501
[29] Gielis J 2003 *Am. J. Bot.* **90** 333–8
[30] Otten S, Kario A, Kling A and Goldacker W 2016 *Supercond. Sci. Technol.* **29** 125003
[31] Connolly C 2009 *Ind. Robot.* **36** 540–5
[32] Wimbush S C and Strickland N M 2016 *IEEE Trans. Appl. Supercond.* **27** 8000105
[33] Dam M, Burger W J, Carpentiero R, Chesta E, Iuppa R, de Rijk G and Rossi L 2022 *IEEE Trans. Appl. Supercond.* **32** 4500105